Controls on Polar Southern Ocean Deep Chlorophyll Maxima: Viewpoints from Multiple Observational Platforms

Philip W. Boyd[1,2,3], David Antoine[4], Kimberley Baldry[1], Marin Cornec[5], Michael Ellwood[6,7] Svenja Halfter[1,8], Leo Lacour[1,9], Pauline Latour[1,3], Robert F. Strzepek[1,2], Thomas W. Trull[10], Tyler Rohr[1,10]

Submitted to Global Biogeochemical Cycles 7 June 2023

[1]Institute for Marine and Antarctic Studies, University of Tasmania, Hobart, TAS, Australia

[2]Australian Antarctic Program Partnership (AAPP), Institute for Marine and Antarctic Studies, University of Tasmania, Hobart, TAS, 7001, Australia

[3]ARC Australian Centre for Excellence in Antarctic Sciences (ACEAS), University of Tasmania, Hobart, TAS, 7001, Australia

[4]School of Earth & Planetary Sciences, Curtin University, Perth, WA 6845, Australia

[5]School of Oceanography, University of Washington, Seattle, WA, USA

[6]Research School of Earth Sciences, Australian National University, Canberra, ATC, Australia.

[7]Australian Centre for Excellence in Antarctic Science (ACEAS), Australian National University, Canberra, ATC, Australia

[8]NIWA Wellington, 301 Evans Bay Parade, Hataitai, Wellington 6021, New Zealand

[9] CNRS & Sorbonne Université, Laboratoire d'Océanographie de Villefranche, LOV, Villefranche-sur-Mer, France,

[10]CSIRO Environment, Hobart, TAS 7004, Australia

Formatted: Numbering: Continuous

Abstract

Deep Chlorophyll Maxima (DCMs) are ubiquitous in low-latitude oceans, and of recognized biogeochemical and ecological importance. DCMs have been observed in the Southern Ocean, initially from ships and recently from profiling robotic floats, but with less understanding of their onset, duration, underlying drivers, or whether they are associated with enhanced biomass features. We report the characteristics of a DCM and DBM (Deep Biomass Maximum) in the Inter-Polar-Frontal-Zone (IPFZ) south of Australia from CTD profiles, shipboard-incubated samples, a towbody, and a BGC-ARGO float. The DCM and DBM were ~20 m thick and co-located with the nutricline, in the vicinity of a subsurface ammonium maximum characteristic of the IPFZ, but ~100 m shallower than the ferricline. Towbody transects demonstrated that the co-located DCM/DBM was broadly present across the IPFZ. Large healthy diatoms, with low iron requirements, resided within the DCM/DBM, and fixed up to 20 mmol C m^{-2} d^{-1}. The BGC-ARGO float revealed the DCM/DBM persisted for >3 months. We propose a dual environmental mechanism to drive DCM/DBM formation and persistence within the IPFZ: sustained supply of both recycled iron within the subsurface ammonium maxima and upward silicate transport from depth. DCM/DBM cell-specific growth rates were considerably slower than those in the overlying mixed layer, implying that phytoplankton losses are also reduced, possibly as a result of heavily silicified diatom frustules. The light-limited seasonal termination of the observed DCM/DBM did not result in a 'diatom dump', rather ongoing diatom downward export occurred throughout its multi-month persistence.

Plain language summary

- DCMs and DBMs are typically observed in the low latitude ocean where they contribute to regional ecology and biogeochemistry.

- They are cryptic features not observable from satellites.
- They are being more frequently observed in the Southern Ocean due to increased deployments of robotic profilers.
- The mechanisms that lead to their formation are not well understood in the Southern Ocean.
- Little is known about their seasonality or biogeochemical role.
- We use multiple observational platforms to address these issues.

1. Introduction

Deep Chlorophyll Maxima (DCMs) were initially observed in the low-latitude oligotrophic ocean, where they were conspicuous in vertical fluorescence profiles at the base of the seasonal thermocline and upper portion of the nitracline (Cullen, 1982; Cullen, 2015; Hogle et al., 2018). These features have subsequently been observed in other basins, including the Southern (S.) Ocean (Holm-Hansen and Hewes 2004; Parslow et al., 2001; Trull et al., 2001), during oceanographic surveys such as WOCE (World Ocean Circulation Experiment). In the last decade, the deployment of robotic profiling floats has revealed that DCMs are widespread features across the global ocean (Cornec et al., 2021a). The frequent sampling by such floats has provided insights into the seasonality of DCMs (Cornec et al., 2021a; Bock et al., 2022).

DCMs are best characterized in the low-latitude ocean, often using a comparison of physical, chemical and bio-optical vertical profiles (Cullen, 2015). Other insights have come from discrete sampling of the subsurface feature and shipboard manipulation experiments to elucidate their environmental controls (Hopkinson et al., 2005; Hogle et al., 2018). This multi-faceted research allowed the determination of several factors controlling DCMs: a well-stratified seasonally-stable thermocline, sufficient irradiance for phytoplankton growth along with contact with the nitracline, often via internal waves (Cullen, 2015). Under the classification of DCMs developed by Cornec et al. (2021a), these low-latitude persistent features are termed Typical Stable Water Systems (see Cullen, 2015). Low-latitude DCM habitats are dominated by specialised phytoplankton groups such as picophytoplankton (Cullen, 2015). These communities typically exploit the episodic supply of additional nutrients and hence can play both an important ecological and biogeochemical role, such as in fuelling additional downward export flux (Pollehne et al., 1993).

In the last decade, the deployment of profiling robotic floats with a range of bioptical sensors (such as chlorophyll (Chl) fluorescence and backscatter) in oligotrophic and other oceanic regions has enhanced our ability to classify these subsurface features (Cornec et al., 2021a; Strutton et al., 2023). Some DCMs have co-located Deep Biomass Maxima (DBMs) whereas others have no DBM but result from a photoacclimatory increase in cellular Chl to harvest light at depth. The ocean-wide coverage of robotic profiling floats has also provided insights into the geographical distribution and typology of DCM/DBMs (Cornec et al., 2021a; Bock et al., 2022).

For other DCM categories reported in Cornec et al. (2021a), a diverse range of drivers has been developed from both observational and experimental studies, that differ from the classical model of light/nitrate and picophytoplankton for the oligotrophic ocean (Cullen, 2015). For example, (new) iron and light are key controls on the resident picoeukaryotes and diatoms in DCM/DBMs in the North Pacific (Hopkinson et al., 2005). The supply of regenerated nutrients has also been invoked as a driver for (diatom-dominated) DCM/DBMs in the Mediterranean Sea (Marañón et al., 2019). For other regional diatom-dominated DCM/DBMs, silicate and/or iron supply from underlying waters have been proposed as candidate drivers (Hopkinson & Barbeau, 2008; Allen et al., 2005; Yool & Tyrrell, 2003). Mesoscale eddies can also play a role in DCM/DBM formation (Cornec et al., 2021b; Strutton et al., 2023). In some oligotrophic regions, photoacclimation alone can be the driver that underpins the presence of DCMs (Barbieux et al., 2019). For the S. Ocean, Pinkerton et al. (2021), using data from three BGC-ARGO floats, advocate using a new metric - the irradiance at the base of the mixed layer - to explain the magnitude of DCMs.

In the S. Ocean, proposed drivers of DCM/DBM formation include silicate resupply from the nutricline (Parslow et al., 2001), and 'irregular fertilization' by iron (Cornec et al., 2021a), potentially via eddies (Uchida et al., 2020) since the DCM/DBM depth is typically shallower than that of the ferricline (Klunder et al., 2011). S. Ocean DCM/DBMs also differ from those in other regions in that they are only observed - by floats - over a few months during austral summer (see Figure 4 in Cornec et al., 2021a) and their magnitudes are typically smaller (see S-Figs. 20 and 21 in Cornec et al., 2021a). These puzzling features have been classified as 'Ghost Zones' by Cornec et al. (2021a) because a suite of outstanding questions remains regarding the drivers of initiation, longevity, fate, and biogeochemical roles of S. Ocean DCM/DBMs. Here, we employ 3 distinctive approaches: ship Conductivity–Temperature–Depth (CTD) profiles and rosette sampling, towbody surveys, and high temporal resolution BGC-ARGO profiles to jointly explore the underpinning mechanisms, spatial bounds, environmental controls, links to the DBM and seasonality of the S. Ocean DCM. This, in turn, enables us to begin to probe the biogeochemical and ecological roles of S. Ocean DCM/DBMs.

2.1 Materials and Methods

The data presented here were obtained during the 42 day SOLACE (Southern Ocean Large Area Carbon Export) voyage on the RV Investigator (IN2020_V08) from 6 December 2020 to 15 January 2021 to the S. Ocean, along with several months of observations from a robotic profiling BGC-ARGO float deployed at a polar site (55.48°S 138.5°E) during this voyage. SOLACE occupied three sites, one in the subantarctic (47.1°S, 141.4°E) near the Southern Ocean Time Series (SOTS) station, and two south of the Polar Front (55.8°S 138.5°E, 57.8°S 141.5°E, S-Figure 1). The results presented here focus only on the two polar sites, both sampled in a quasi-Lagrangian mode following the deployment of a holey-sock drogue at the

mid-depth of the seasonal mixed layer. The drogue drift trajectory over 10 days at the 55.8°S site is presented in S-Figure 2. The trajectory was typical of the low advective regimes we sought, and was similar to that observed at the southern site.

At each polar site, vertical oceanographic profiles were obtained using a Sea-Bird SBE911-plus CTD unit (conductivity, temperature, and depth) that was linked to calibrated fluorometer (Chelsea Aqua-Tracker Mk3), oxygen (SBE 43 electrode), photosynthetically active radiation (i.e., PAR, Biospherical Laboratories) and transmissometer (Wetlabs C-Star 700 nm) sensors. Mixed Layer Depths were computed for each CTD profile using the mean of a density threshold and density gradient algorithm. For the threshold, we followed Boyer Montegut et al.'s (2004) criteria (via Holte and Talley, 2009): a density difference of 0.03 kg m^{-3} referenced to the closest measurement to 10 dbar. For the mixed layer gradient, we followed Dong et al. 2007 (via Holte and Talley, 2009) where the gradient criterion was 0.0005 kg m^{-3} $dbar^{-1}$.

The CTD and associated instruments were mounted within the frame of a 24 bottle (12 L) rosette sampler. The CTD sensor package was calibrated after Kwong et al. (2020). Seawater was sampled from the rosette at selected depths for nutrients and rate measurements (including iron uptake, see later). Dissolved macronutrients were analysed following procedures in Rees et al. (2018). Seawater samples for trace metal and isotope determination were collected using acid-cleaned, Teflon-coated, externally-sprung, 12 L Niskin bottles attached to an autonomous rosette equipped with a Sea-Bird SBE911-plus CTD unit following methods detailed in Ellwood et al. (2020a,b). Particulate trace metal samples were collected in situ onto acid-leached 0.2-µm PVDF (142 mm diameter) filters (Sterlitech) using six large-volume dual-head pumps (McLane Research Laboratories), deployed at various

water depths (Ellwood et al., 2020a,b). Elemental analysis for dissolved and particulate trace metals followed procedures in Ellwood et al. (2020b). Discrete Particulate Organic Carbon (POC) samples were analysed following Trull et al. (2018). The POC data were used to calibrate the CTD transmissometer. In-situ values from the instrument were averaged across all depths within 5 m (above or below) of the Niskin bottles from which the discrete POC samples were obtained. Beam attenuation, c (m^{-1}) was computed from the transmissometer as

$$c = -(1/.25) * \ln(trans/100)$$

where trans is the beam transmittance (%). The beam attenuation from particulates (c_p) is estimated by subtracting out the attenuation due to the intrinsic properties of seawater (c_{sw}), $c_p = c - c_{sw}$.

c_{sw} is set using the minimum value measured by the sensor at depth, assuming particle-free seawater. An estimate of the proportion of detrital (i.e., non-phytoplankton) POC was obtained by assuming a carbon (C) to Chl ratio of 30 (g:g) in living phytoplankton (Strutton et al., 2023), such that

Detrital Fraction = POC – 30*Chl).

Water from the trace metal rosette was also obtained for biological and biogeochemical metrics. Extracted Chl, photochemical efficiency (F_v/F_m), and the functional absorption cross section (σ_{PSII}; nm^2 reaction centre $(RC)^{-1}$) of photosystem II (PSII) were measured after Boyd et al. (2022). Biogenic silica (BSi) was determined by measuring silicic acid spectrophotometrically after converting BSi to silicic acid through leaching with 0.1 M sodium hydroxide at 85°C for 2.25 h (Paasche 1973). Samples from multiple depths across the seasonal mixed layer and DCM/DBM were incubated in shipboard temperature-controlled (± 0.5 °C) seawater incubators, with light depths mimicked using a range of neutral density screening. Daily rates of Net Primary Production (NPP) and iron uptake were measured for

0.2-2 μm, 2-20 μm, >20 μm size fractions and the community (>0.2 μm) following procedures in Boyd et al. (2022). NPP was calculated from non-titanium-washed filters, as titanium decreased carbon (C) uptake rates by ~ 15%. However, iron (Fe) and Fe:C uptake rates were calculated using titanium-washed Fe and C samples, and so are intracellular. Six light depths were chosen to provide coverage across the mixed layer and within the underlying DCM. The 1% I_o (surface irradiance) ranged from 83-92 m depth (with an attenuation coefficient (K_d) ~0.05).

The Triaxus towbody (MacArtney A/S, Esbjerg, Denmark) was towed at ~9 knots (using ~ 800 m of conducting core cable). It was undulated from ~15–200 m depth to observe the co-located DCM and DBM. We investigated measurements from a suite of sensors on the towbody including nitrate (SUNA UV-spectrometer, SBE), oxygen (SBE 43 electrodes plumbed in line with the CTD intakes) duplicate Sea-Bird SBE911 CTDs and a calibrated Sea-Bird ECO-Triplet FLBBCD2K measuring Chl fluorescence (470/695nm excitation/emission), optical backscatter (700nm), and dissolved organic matter fluorescence (370/460 nm – not discussed here) (Sea-Bird Electronics, Bellevue, USA). All data from these instruments were integrated over 2-s intervals. The estimation of the mixed layer depth was as for the CTD profiles. Profiles from each up/down Triaxus profile were smoothed with a 10 m moving average. A DCM was identified when the maximum Chl concentration was below the mixed layer depth (MLD) and >10% greater than the mixed layer depth Chl mean value. The thickness of the DCM is based on the region with at least 50% of the difference between the MLD mean and maximum Chl value. This method was also applied to the identification of a DBM using the POC field measured by the transmissometer using the same calibration as described for the CTD. We employ the term ‘deep enhancement’, which is defined as the percentage increase of the DCM mean (averaged across the thickness of DCM)

relative to the MLD mean. Deep enhancement of POC and C:Chl are computed within the DCM, rather than independently defining a DBM and D(C:Chl)M, respectively, with potentially different vertical boundaries.

A BGC-ARGO robotic profiling float (Provor-CTS5 float (NKE)), WMO 5906624, was deployed at the 56°S site during our voyage. It had the following sensor constellation: a SBE41 CTD (Sea-Bird); an ECO-Triplet composed of a Chl *a* fluorometer (excitation at 470 nm; emission at 695 nm), a Colored Dissolved Organic Matter (CDOM) fluorometer, and an optical backscattering sensor at 700 nm and angle of 124° (bbp); an OCR-504 (Satlantic) radiometer measuring PAR integrated over 400-700 nm; a SUNA-V2 nitrate sensor (Satlantic); a Seafet pH sensor (Sea-Bird); an Anderaa optode-4330 for dissolved oxygen, and an Underwater Vision Profiler (UVP) version 6. The float was programmed to profile every 2-4 days from December to late March and thereafter every 10 days, with parking depths of 500 or 1000 m. Following Argo protocols, hydrological data collected by the SBE41 Seabird CTD sensors were processed and quality-controlled, as described by Wong et al. (2023). Bio-optical adjusted data were used after quality-control following Schmechtig et al. (2014) for Chl fluorescence, and Schmechtig et al. (2019) for the bbp. Chlorophyll *a* values were multiplied by a S. Ocean specific correction factor of 0.3 following Ardyna et al. (2019). The bbp was converted to POC using the S. Ocean specific relationship reported in Johnson et al. (2017). Phytoplankton carbon (C) was then derived assuming a contribution to POC of 30% (Behrenfeld et al. 2005). Chlorophyll *a* and bbp were partitioned into 4 components following Briggs et al. (2020): small, labile fluorescing ($chla_s$) and backscattering (bbp_s) particles; and large, fast-sinking fluorescing ($chla_l$) and backscattering (bbp_l) particles. The division between small and large corresponds approximately to a particle chlorophyll content of 60 pg for $chla_s$ versus $chla_l$ and a particle diameter of 100 μm for bbp_s

versus bbp_l. Data are available through the Coriolis database (ftp://ftp.ifremer.fr/ifremer/argo; Argo, 2000). The float data were collected and made freely available by the International Argo Program and the national programs that contribute to it (https://argo.ucsd.edu, https://www.ocean-ops.org). The Argo Program is part of the Global Ocean Observing System.

2. Results

3.1 Ship-based sampling

A combination of data from CTD profiles and discrete chemical sampling provides a broader oceanographic context with which to interpret the location of the DCM/DBM feature. Two sites were occupied for multiple days at 55.48°S 138.34°E (hereafter referred to as 56°S) and further to the SE at 58°S 141°E (hereafter referred to as 58°S) in late December 2020 and early January 2021 during the SOLACE voyage (S-Figure 1). Each site was selected using 3 day composite satellite maps of Chl concentrations overlaid on sea surface height anomaly (S-Figure 1b), and low advective sites with elevated Chl stocks were sought. At 56°S, the water column was characterised by temperature/salinity properties of the IPFZ (Parslow et al., 2001), including a temperature minimum (Tmin) layer between 100 and 300 m depth (Figure 1a).

A DCM was evident at 56°S as a >20 m thick feature in Chl fluorescence (Figure 1d) co-located with the upper strata of the Tmin layer and associated with low underwater irradiances (Figures 1a, 1c). The DCM was co-located with a DBM across all 10 profiles, indicative of biomass accumulation (Figure 1e), however, a coincident decrease in the C:Chl ratio points to photoacclimation at depth as well (Figure 1f). The proportion of detrital POC was ~0.9 in the mixed layer and decreased to ~0.7 in DCM/DBM (Figure 1g). This subsurface feature was observed at the base of the seasonal thermocline in the zone where

293 both nitrate (from 25 to ~28 μmol L^{-1}) and silicate (from 4 to >10 μmol L^{-1}) concentrations
294 increased with depth (Figures 2b and 2e). However, the DCM was not co-located with the
295 ferricline (~0.2 nmol kg^{-1} dissolved Fe (dFe) in the DCM c.f. >0.4 nmol kg^{-1} at depth, Figure
296 2a). The DCM/DBM feature was coincident with a subsurface ammonium maximum in all
297 profiles where ammonium was sampled (Figure 2c). The Tmin layer, a relict feature from
298 winter water, is often associated with a subsurface ammonium maximum that is present
299 during winter in the IPFZ (Mdutyana et al., 2021).
300
301 Discrete samples from the CTD rosette were analysed for biological metrics such as BSi
302 (Figure 2h), floristics (not shown), F_v/F_m (Figure 2i), and NPP/Fe uptake rates (Figures 2k
303 and 2l). Extracted Chl measurements confirmed the presence of a DCM (>0.7 mg m^{-3} c.f. 0.2
304 mg m^{-3} within the mixed layer, Figure 2g). At the 56°S site BSi was measured at ~0.1 μmol
305 L^{-1} in the mixed layer, but increased to 0.2 μmol L^{-1} within the DCM – indicative of a
306 diatom-dominated subsurface feature (Figure 2h). The DCM/DBM was collocated with a
307 deep particulate phosphorus (P) maximum (80 nmol kg^{-1} c.f ~30 nmol kg^{-1} in the mixed layer,
308 data not shown) but was only associated with a small increase in particulate Fe stocks (0.1
309 nmol kg^{-1} in the DCM, c.f. <0.1 nmol kg^{-1} in the mixed layer, data not shown).
310
311 Light microscopy revealed that the DCM/DBM was dominated by large diatoms comprising
312 many species (S-Figure 3). Cells in the subsurface feature had an F_v/F_m of ~0.5, whereas
313 those in the mixed layer had either equivalent or lower values (Figure 2i). The functional
314 absorption cross section of PSII (σ_{PSII}) was variable and ranged from 600-1500 nm^2 RC^{-1}
315 across two profiles (Figure 2j). Carbon (i.e., NPP) and Fe (by phytoplankton and
316 heterotrophic bacteria) uptake profiles (Figures 2k, 2l) exhibited low iron uptake rates within
317 the DCM/DBM (~2 pmol L^{-1} d^{-1}, c.f. up to 40 pmol L^{-1} d^{-1} in the mixed layer) with large cells

318 contributing ~60% to the community integrated rate at depth (Figure 3). In contrast, NPP was
319 ~0.3 μmol L^{-1} d^{-1} in the DCM/DBM (c.f. 0.7-0.8 μmol L^{-1} d^{-1} in the mixed layer, Figure 2k).
320 Large cells (>20 μm) dominated C uptake in both the mixed layer and DCM (Figure 3),
321 resulting in low Fe:C uptake ratios (3.3-4.5 μmol:mol), indicative of cells in steady-state.
322
323 In contrast, at the 58°S site there was no evidence of a DCM or DBM until almost the end of
324 our site occupation (Figure 4d, 4f), with relatively high Chl stocks (0.6 mg m^{-3} (extracted
325 value) within the seasonal mixed layer (Figure 5g and S-Figure 4). From a physical
326 perspective, ship-based sampling revealed that the water column had a colder (1-1.2°C) and
327 deeper (225-275m depth, Figure 4a) Tmin feature than at the 56°S site (1.75-2.0°C and
328 ~200m depth, Figure 2a). Importantly, both features overlie a 2.5°C layer of Upper
329 Circumpolar Deep Water (UCDW) suggesting similar winter water mass initial composition
330 (data not shown). Biogeochemically, detrital POC made up a smaller proportion (~0.8) in the
331 surface mixed layer at 58°S (Figure 4g) relative to the 56°S site (Figure 2g). As at the 56°S
332 site, a subsurface ammonium maximum was evident below the mixed layer (Figure 5c) and
333 coincided with the upper stratum of the Tmin layer (Figure 5a). At the 58°S site, BSi was 0.2-
334 0.3 μmol L^{-1} within the surface mixed layer (Figure 5h), particulate P was 80-120 nmol kg^{-1}
335 in the mixed layer (data not shown) and particulate Fe was variable with depth (0.1-0.4 nmol
336 kg^{-1}, data not shown). Phytoplankton cells exhibited F_v/F_m of ~0.45 in the surface mixed
337 layer (Figure 5i) and a σ_{PSII} of >800 nm^2 RC^{-1} (Figure 5j) in this stratum. NPP rates were
338 higher than at the 56°S site (Figure 3a, 3b), but community Fe uptake rates were comparable
339 (Figure 3c, 3d). As observed for the 56°S site, cells <2 μm dominated Fe uptake while
340 cells >20 μm dominated NPP (Figure 3).
341
342

343 *3.2 Spatial and temporal patterns in the DCM feature around 56°S and 58°S*

344 The spatial extent of the DCM/DBM and the relationship with environmental drivers of this
345 feature around the two sites were explored using Triaxus towbody surveys of around 30-40
346 miles comprising three sections at each site (S-Figure 2c and Figures 6 and 7). An initial
347 Triaxus tow of ~ 35 miles (55.75°S 138.65°E to 138.3°E, S-Figure 2) to the west of the site
348 under darkness (to avoid non-photochemical quenching (NPQ)) exhibited constancy in both
349 the IPFZ water mass characteristics and the location of the DCM (Figure 6). Towbody
350 observations also revealed the presence of a coincident DBM of ~20 m thickness located at
351 80 to >100 m depth. The POC:Chl ratios (note POC will contain non-phytoplankton cells)
352 were typically lower (~40) within the DCM/DBM than in the overlying mixed layer (~80)
353 reflecting the greater contribution of Chl to this feature relative to POC (Figure 6 c.f. 1f).
354
355 Several additional tows at the 56°S site further corroborated that the DCM was a more
356 widespread feature beyond our study site (Figure 6). However, there was some spatial
357 variability along each leg of the Triaxus tows in both the depth, thickness and magnitude of
358 the DCM. The relationship with the depth and thickness of the DCM relative to that of the
359 DBM provides clues as to the environmental forcing of this feature on short temporal and
360 spatial scales. The depth of the DCM and DBM were well correlated and generally co-located
361 (within ~5 m) during all tows that identified both a DCM and DBM. However, the DCM was
362 consistently slightly deeper (~5 m) than the DBM, suggesting the increasing role of
363 photoacclimation with depth. The thickness of the DCM and DBM were also well correlated,
364 with the DCM typically ~5 m thicker than the DBM. The absolute magnitude of the DCM
365 and DBM were generally well correlated, however the deep enhancement of the DCM was
366 greater than that of the DBM (data not shown).
367

368 At the 58°S site, there was evidence of temporal evolution of a co-located DCM and DBM
369 near the study site. This emerging feature is conspicuous on January 11 2021 on tow 2 (i.e.,
370 the S-N return leg to the 58°S study site (Figure 7 and S-Figure 2c). During the first
371 deployment at 58°S, the DCM thickness was much more variable than that of the DBM. A
372 comparison of the features at both sites revealed that the absolute magnitudes of the DCM
373 and DBM were larger at 58°S than 56°S, whereas the deep enhancement of the DCM and
374 DBM was substantially larger at 56°S compared to 58°S (S-Figure 4). At 56°S Chl was
375 enhanced by 1 to 4 fold across the DCM relative to the surface mixed layer, coincident with a
376 smaller but substantial 20-60% enhancement of POC. In contrast, at 58°S deep enhancement
377 of Chl and C did not exceed ~25% in any profile. If the emerging DCM/DBM observed at the
378 58°S is to be interpreted as a precursor to the more established feature observed as 56°S then
379 this suggests that subsurface biomass accumulation already exists below the mixed layer at
380 58°S (even more so than at 56°S) but does not emerge as a maximum relative to the surfacer
381 layer until overlaying phytoplankton stocks are grazed to levels lower than in the subsurface
382 feature.
383
384 The seasonality and downward export potential of the DCM observed in the IPFZ at the 56°S
385 site were explored using the BGC-ARGO float. The float datasets extended the week-long
386 shipboard observations for 3-4 months within the IPFZ water mass (S-Figure 2a) and thus can
387 be cautiously linked to shipboard trends presented in Figures 1,2 and 5. The float's multi-
388 sensor constellation provides insights into temporal evolution of physical (Figure 8) and bio-
389 optical (Figure 9) properties over the ensuing months from austral summer into autumn/fall
390 2021, allowing us to track changes in the characteristics of the DCM/DBM (thickness,
391 POC:Chl, depth) and its environment. The distinctive DCM/DBM feature we observed from
392 CTD profiles (Figure 1) and the Triaxus tow-body (Figure 7) was also evident from the BGC-

ARGO float observations for ~3 additional months. The joint presence of the DCM and DBM spanned late December 2020 to late March 2021 (Figure 9a,b) and exhibited a comparable gradient in C:Chl ratios, which decreased with depth (Figure 9c,d) as observed with the towbody (Figure 6). There was no marked change in the POC:Chl ratio in the DCM over several months (Figure 9c), which we interpret as indicative of a persistent healthy population of large diatoms, based on the float profiles obtained during our shipboard occupation of this site.

The magnitude (~0.6 μg L^{-1}, Figure 2g, c.f. Figure 1d and (a), depth (80-100 m) and thickness (20-25 m) of the subsurface feature were largely consistent for 3 months (Figure 9) despite pronounced changes in the depth of the surface mixed layer, which varied from <50 m to ~100 m depth (Figure 8). The DCM/DBM decreased in amplitude and thickness in late March, which coincided with a programmed change in the sampling frequency of the float from 2 to 5 days (for several profiles) and followed by a shift to 10 day intervals (i.e., ARGO standard protocol). The cause of the demise of the DCM/DBM feature is unclear but may be linked to the threefold seasonal decrease in incident irradiance in April 2021 that is reflected in underwater PAR of <2 μmol quanta m^{-2} s^{-1} within the subsurface feature (S-Figure 5).

The fate of the large diatoms within this feature is also unclear. There was no evidence of a distinct downward particle pulse in either the BCG-ARGO Chl or POC time-series associated with the decline of the DCM/DBM feature (Figure 10). However, there is some evidence of a small but constant flux of particles, from January to March 2021, from the backscatter sensor on the float (Figure 10b) that is less conspicuous in the float fluorometer time-series (Figure

417 10a). This observation suggests that the diatoms residing within the subsurface features may
418 have sunk to depth intact as both cells and empty frustules.
419
420 **4. Discussion**
421 The different observational modes we employed to study the DCM within the IPFZ along
422 with the diverse range of metrics, from biogeochemical to photo-physiological, enable us to
423 probe many facets of this polar subsurface feature. We explore potential drivers for the DCM
424 formation, then compare and contrast it's characteristics with the biogeochemical fluxes we
425 measured. Next, we further interpret towbody and BGC-ARGO observations to examine its
426 wider-scale spatial and temporal distribution. The float data also enable us to address
427 questions about it's longevity and fate. Together, these multiple lines of examination provide
428 insights into the DCM's ecological and biogeochemical role in the S. Ocean.
429
430 *4.1 Drivers of DCM/DBM formation*
431 We observed the DCM feature in late December after arriving at the 56°S site, but prior
432 studies have recorded a springtime DCM (Parslow et al., 2001), suggesting that the 56°S
433 feature may have formed before December. The earliest seasonally reported DCM in the S.
434 Ocean was in November 1995 at 53°S i.e., at the northern edge of the IPFZ, the most
435 southern station sampled by Parslow et al., 2001). They reported a diatom-dominated feature
436 at ~65 m depth, that was not present in a prior October 1991 transect in the IPFZ. Parslow et
437 al. (2001) reported data on Chl and pigments but not for backscatter or transmissivity so it is
438 not known if there was also a DBM in the spring 1995 feature. However, they did present
439 values of alpha (the slope of the phytoplankton photosynthesis-irradiance curve) that were
440 two-fold higher in the DCM phytoplankton community compared to overlying waters,
441 suggesting a low light-acclimated phytoplankton population, and hence potentially no DBM.
442 The November 1995 feature Parslow et al. observed had 0.7 μg Chl L^{-1} (c.f. 0.3 μg L^{-1} in the

443 overlying surface mixed layer) and it was present at a time when mixed layer silicate and
444 nitrate were close to winter reserve concentrations (i.e., likely not limiting).
445
446 Here, we attempt a space-for-time substitution to explore whether the 58°S site, which was at
447 an earlier stage of the seasonal productivity cycle (Figure 2 c.f. Figure 5; S-Figure 6) can be
448 viewed as a potential precursor for DCM formation. The 58°S site which had similar IPFZ
449 physical characteristics, such as the Tmin layer (Figure 4a), may provide insights regarding
450 what factors, such as resource limitation, led to the formation of a DCM/DBM (see Lande et
451 al., 1989). In contrast, at our polar sites which were more southerly (56°S and 58°S) than that
452 studied by Parslow et al. (2001) in November 1995, silicate concentrations were low and
453 vanishingly low in the surface mixed layer of the 56°S and 58°S, respectively (Figures 2 and
454 5). Parslow et al. (2001) also reported low silicate concentrations (along with DFe of 0.2
455 nmol kg^{-1}) in DCMs near 54°S (i.e., within the IPFZ) in January over several different years.
456 At both our sites, DFe was ~0.2 nmol kg^{-1} (Figures 2 and 5) suggesting Fe stress, based on
457 the relationship between DFe concentration and F_v/F_m reported for the polar S. Ocean in
458 Boyd and Abraham (2001). Furthermore, at the 56°S and 58°S sites, Chl and (NPP) in the
459 mixed layer were 0.3 mg m^{-3} (~600 mg C m^{-2} d^{-1}) and 0.6 mg m^{-3} (~1000 mg C m^{-2} d^{-1})
460 (Figures 2 and 5), respectively, supporting the conclusion from the ocean colour remote-
461 sensing (S-Figure 6) that the 58°S site was at an earlier stage of development in its seasonal
462 primary productivity cycle.
463
464
465 At the 58°S site, based on drawdown in silicate between the two profiles (obtained while
466 tracking a holey sock drogue, and so quasi-Lagrangian), 4 days apart (Figure 5h), the demand
467 for silicate is 0.176 µmol L^{-1} d^{-1}, which is ~5-fold lower than the rate measured for the Pacific

sector of the S. Ocean, ~1 μmol L^{-1} d^{-1} (Sigmon et al., 2002) at a similar latitude. This, along with low and decreasing silicate stocks, suggests that cells at this site are close to Si limitation. Thus, it is likely that the 58°S site would be on the verge of transitioning to a decline in phytoplankton stocks and NPP driven by silicate and/or Fe limitation. These conditions may have enabled the development of a DCM/DBM (see DCM/DBM in S-N tow on 11 January 2021 in Figure 7) around mid-January 2021 (i.e., at the end of our ship-based observational record at the 58°S site).

How did the subsurface feature develop and where was it initiated within the water column? The gradual enhancement of the subsurface features evident in S-Figure 4, assuming it was in the same water mass, suggest that a DCM and DBM evolved at depth at a time when there is high chl in overlying waters and a correspondingly high light attenuation coefficient. As such it suggests the hypothesis put forward by Cornec et al. (2021a) on DCM formation - in which there is *in situ* enhancement of the DCM/DBM driven by reduced light attenuation at depth due to the decline of the stocks in the mixed layer - does not fit this S. Ocean scenario. Furthermore, in the surface mixed layer the estimated phytoplankton turnover times based on POC stocks and NPP (S-Table 1) are higher than in the DCM, despite the onset of Fe and/or Si limitation. This suggests that the build-up of the subsurface feature must require low loss terms, in particular low loss rates due to herbivory. The resident large diatoms present at the 56°S site have highly silicified frustules (S-Figure 3) thought to be an evolutionary mechanism to prevent/minimize grazing (Smetacek, 2001) and evident in their ability to resist salp herbivory (S-Figure 7). Thus, a combination of bottom-up (onset of silicate and/or Fe limitation in the surface mixed layer) and top-down (low loss terms to grazers) may lead to the onset of DCM/DBM formation, but whether this formation takes place at depth, or originates within the mixed layer via the relocation of a subset of the phytoplankton

493 population (the large diatoms) via slow sinking/buoyancy regulation , remains an open
494 question.
495
496 In the next section, we explore key characteristics of the DCM observed at the 56°S site such
497 as phytoplankton species composition and Fe uptake rates to further explore whether the
498 conditions at the 58°S site, at the time of occupation, led to DCM/DBM formation.
499
500
501 *4.2 DCM/DBM characteristics and biogeochemical fluxes*
502 The feature at 56°S had several distinctive characteristics that enable us to further probe the
503 validity of silicate and/or Fe limitation as key environmental triggers in the initiation of a
504 DCM. The subsurface phytoplankton assemblage differed from that in the overlying water
505 column (S-Figure 3). Based on light microscopy, the DCM/DBM was dominated by large
506 diatoms, many >200 μm in length, comprising multiple species (see S-Figure 3). Multiple
507 diatom species have also been recorded in a DCM in the Indian sector of the S. Ocean by
508 Gomi et al. (2010). At our 56°S site, observations from microscopy are supported by a >3-
509 fold higher BSi concentration in the DCM relative to the overlying mixed layer (Figure 2h).
510 Size-fractionated NPP and Fe uptake revealed that the large cells (>20 μm fraction)
511 dominated NPP within the DCM (0.1 μmol L^{-1} d^{-1}) (Figure 3), had a relatively high
512 photosynthetic competence (F_v/F_m, Figure 2i c.f. theoretical maximum of 0.65 see Boyd and
513 Abraham, 2001), and very low Fe requirements at 56°S (Figure 3b). These low Fe
514 requirements for large polar diatoms are also observed in lab cultures and are attributed to the
515 cells' ability to increase the size of their light-harvesting antenna under low light conditions
516 (with implications for self-shading, see later) rather than increase the number of photosystem
517 units in the chloroplast, which has an added Fe cost for effective light harvesting under low

518 irradiances (Strzepek et al., 2012). Irradiances at the base of the DCM were low during the
519 daytime (1-20 μmol photons m^{-2} s^{-1}, Figure 1c and S-Figure 5b) suggesting that large polar
520 diatoms may be particularly well suited to persist in the poorly-lit DCM relative to other
521 species with higher iron requirements a such low irradiances.
522
523 The findings of a shipboard perturbation experiment conducted at the 56°S site in which dFe,
524 manganese and irradiance were amended either alone or in combination (Latour et al., in
525 prep.) reveal some evidence of Fe limitation of the resident cells within the DCM/DBM.
526 Although some of the treatments, such as increasing both Fe and irradiance, do not reflect
527 conditions within the overlying mixed layer at 56°S, these perturbations do provide valuable
528 insights into the physiological status of the cells within the DCM/DBM. The transfer of
529 resident cells to more optimal conditions (high irradiance and high Fe) led to a major
530 upregulation in their physiology, as evidenced by marked increases in Chl, POC and BSi
531 stocks (relative to a high light only treatment). Thus, diatoms are probably subsisting in the
532 DCM/DBM with sufficient resources for low rates of NPP (Figure 3) in a subsurface niche
533 that enables them to continue to be productive for months. However, the perturbation
534 experiments by Latour et al. (in prep.) strongly suggest that these cells remain primed for
535 more optimal conditions (such as nutrient replete and high light, where they could grow faster
536 (S-Table 1)), as is observed in high-latitude polar regions of the Arctic (Hoppe, 2021) and
537 Antarctic (Kennedy et al., 2019).
538
539 Other characteristics of the 56°S site provide insights into what might lead to the initiation of
540 a DCM/DBM as a niche for large diatoms. The ferricline at the 56°S site was >100 m deeper
541 than the seasonal mixed layer (Figure 1a c.f. 2a), indicating that the observed persistence of
542 the DCM/DBM for months (Figure 9) likely requires another source of Fe, since the ~4 pmol

543 L^{-1} d^{-1} Fe demand by large cells would lead to a cumulative demand of >0.1 nmol L^{-1} $month^{-1}$
544 (assuming this observed Fe uptake rate (Figure 3b) was applicable beyond our site occupation
545 in late December 2020). Where could this Fe be supplied from? Subsurface ammonium
546 maxima reflect the signature of microbial remineralisation in many locales including the S.
547 Ocean (see Mdutyana et al., 2021). So, is it possible that the co-location of the DCM/DBM
548 with the upper zone of the subsurface ammonium maximum (Figure 2) indicates a role in for
549 a recycled Fe iron supply to the diatoms within the DCM/DBM?
550
551 Prior measurements of ammonium and dFe recycling made during an *in situ* particle
552 remineralisation study at 180 m depth in a subantarctic site revealed that 0.78 nmol L^{-1} dFe
553 was released per 0.38 µmol L^{-1} of ammonium produced, equating to a resupply ratio of 2.06
554 nmol L^{-1} dFe per µmol L^{-1} of ammonium released (Bressac, unpublished). The subsurface
555 ammonium maximum was ~0.6 µmol L^{-1} at the 56°S (Figure 2c) and approximates steady-
556 state based on three profiles within 9 days. Assuming a conservative turnover time of 100
557 days for the subsurface ammonium maximum (c.f. Mdutyana et al., 2020), this feature could
558 release ~12 pmol dFe L^{-1} d^{-1}, more than meeting the measured diatom Fe requirements
559 (Figure 3b). The subsurface ammonium feature that characterises the Tmin layer (Figures 2c
560 and 5c) is present over winter when it is already dynamic as reported for the IPFZ in the
561 Atlantic sector by Mdutyana et al. (2021). In other systems, Fe recycling within the
562 DCM/DBM is reported to play a key role, for example in sustaining the diatom-dominated
563 feature in the Mediterranean Sea (Marañón et al., 2019).
564
565 Another candidate mechanism for DCM/DBM formation is the alleviation of diatom silicate
566 limitation, as silicate was at low and vanishingly low levels at the 56°S and 58°S sites,
567 respectively, and the DCM was co-located with a subsurface peak in BSi (Figures 2e, 2h and

Figures 5e, 5h). At 90 m depth, the base of the DCM at 56°S, silicate was present at ~10 μmol L^{-1} (Figure 2e). As the DCM persisted for months after our site occupation (Figure 9), a continuing source of silicate is likely required for this feature's ongoing presence. S. Ocean diatoms have been reported to have a low affinity for silicate, especially south of the Polar Front. For example, Nelson et al. (2001) reported half-saturation constants of > 10 μmol L^{-1} for some species north of the Ross Sea during the AESOPS Joint Global Ocean Flux Study (JGOFS) process study. In the lab, Meyerink et al. (2017) measured a half-saturation constant of 11 μmol L^{-1} for the diatom *Proboscia inermis* and 9 μmol L^{-1} for *Eucampia antarctica* when grown under Fe-replete conditions, so silicate availability may be an issue for larger diatoms that reside in the DCM (S-Figure 3). Thus, increased silicate availability at depth may be a driver, along with Fe supply via recycling, for the formation of a DCM in the IPFZ. Our proposed drivers combine prior suggestions for a role of silicate resupply (Parslow et al., 2001) and 'irregular fertilization' of Fe (Cornec et al., 2021a), but go one step further by more clearly identifying a mechanism for sustained Fe supply via recycled rather than new Fe (from the ferricline) that is linked to the presence of the subsurface ammonium maximum.

4.3 Wider distribution of DCMs/DBMs

DCMs/DBMs are typically sampled opportunistically, and hence most observational records are based on a small number of CTD profiles (see Review by Baldry et al., 2021), along with a wider extrapolation of oceanographic snapshots of DCM features across regions (e.g., Parslow et al., 2001). The availability of both the towbody (night-time only) and BGC-ARGO observations enable us to assess the wider distribution of the DCM/DBM, both around our sampling sites, and also for the BGC-ARGO float after the vessel departed the sites. The tow-body sections reveal that the water mass associated with the IPFZ extended by at least a 15 km radius around our sampling site at ~56°S (Figure 6). There is a strong

coherence along each towbody section in the depth and thickness (~20 m) of both the DCM and DBM. Any small variations in the DCM's depth or thickness were mirrored by that for the DBM, likely reflecting small variations in the depth of the seasonal mixed layer in this region. The C:Chl ratio of the subsurface feature was also relatively constant along each section and was several-fold lower than in the overlying waters. The ratios in the upper ocean were typical of those observed in the seasonal mixed layer (Riemann et al., 1989), whereas the values in the DCM were typical of regions with more subsurface carbon at depth than Chl (Taylor et al., 1997). At the 58°S site, the presence of subsurface features were more variable, reflecting their development towards the end of our site occupation (Figure 7 and S-Figure 4).

The wider distribution of both subsurface features can also be explored, in part, using the BGC-ARGO high-resolution time-series (Figures 8 and 9) as the float remained both in the vicinity of the 56°S site (S-Figure 1a) and within the water mass characteristics of the IPFZ. For example, the Tmin layer at depth is conspicuous in the float time-series observations (Figure 8a). Again, a coherent DCM co-located with a DBM is evident for several months (Figures 9a, 9b). As for the towbody, lower C:Chl ratios were evident in the subsurface feature when compared to those in the overlying waters from profiles obtained under darkness (which were interspersed with noon profiles, as is evident from Figures 9c and 9d). The multi-month float record also provides insights into the longevity and eventual decline of the DCM.

4.4 Fate of the DCM/DBM

Most prior studies of DCMs/DBMs in the S. Ocean have been opportunistic ‘snapshots’ (e.g., Parslow et al., 2001; Trull et al., 2001). Insights into the lifetime of such features have therefore come from inference. For example, Parslow et al. (2001) observed DCMs from

November to March, but they are prescribed profiles as part of WOCE and JGOFS transects that straddled multiple years. A recent compilation of DCMs from Southern Ocean BGC-ARGO floats reveals several cases in which a DCM/DBM was repeatedly observed (Cornec et al. 2021a; this study Figures 11 and 12). These studies provide more examples of extended observations of the DCM and DBM to compare with those from January 2021 to May 2021 when the decline of the DCM was evident (Figure 9).

The sampling of a DCM in March within the IPFZ, south of Australia, by Parslow et al. (2001) pointed to a feature in decline, as evinced by empty diatom frustules in the DCM (Kopczynska et al., 2001), and also no difference between the photosynthetic metric alpha (slope of the PE curve) within the DCM relative to the overlying waters. In contrast, higher alpha values (indicative of photoacclimation) were reported in January (summer) DCMs sampled by Parslow et al.. A major unknown from the Parslow et al. (2001) study is whether the DCMs they observed were also representative of DBMs, but there are some suggestions from the relatively high NPP within the DCM features that they may also have been DBMs. The longer time records from Cornec et al. (2021a) reveal for two floats within the IPFZ (Figures 11 and 12) that both DCMs and DBMs were evident in BGC-ARGO time-series observations below the seasonal mixed layer to a depth of ~80 m (i.e., 30 m thick features) in the vicinity of 120°E (WMO # 6901581) for ~55 days (30 December 2016 to 24 February 2017) and near 165°E (WMO # 6901004) for ~60 days (29 Dec 2016 to 03 March 2017). The fate of these features – a decline in late March and no evidence of a particle export pulse - appears similar to that of the DCM/DBM recorded by the float near the 56°S site in the present study (Figure 9 c.f. Figure 12).

642 At the 56°S site, the subsurface feature persisted until mid-April 2021, with coherence
643 between the thickness and depth strata of the DCM and DBM, along with little change in
644 C:Chl ratios in the subsurface feature (Figure 9). The latter is indicative of a healthy
645 population of diatoms and hence a strong indication of a region in which of NPP persisted,
646 albeit at lower rates (see Figure 3). The decline of the DCM was relatively abrupt (likely
647 driven by vanishingly low light levels, S-Figure 5b), and there was no evidence of a late-
648 season fall-out of the large diatoms to depth, as has been speculated by Queguiner (2013) and
649 Kemp (2000). The decline was likely driven by a decrease in underwater solar radiation,
650 which declines markedly in this polar region to <3 µmol photons m^{-2} d^{-1} (S-Figure 5). Prior to
651 April, there was no clear trend in the column-integrated irradiances recorded on profiles by
652 the float at 56°S (S-Figure 5a). What was the fate of the large diatoms within the DCM?
653
654 During our occupation of the 56°S site in late December 2020/early January 2021, there was
655 evidence of grazing by salp swarms but no change in the DCM characteristics over this
656 period. Microscopic analysis of dissected salp guts revealed some large diatoms, but they
657 were intact and likely passed through the gut (S-Figure 7). The likely fate of the diatoms
658 within the DCM may have been a slow but continuous export of a fraction of the assemblage,
659 given that the feature appeared stable and viable for months (Figure 9), as opposed to an
660 export pulse which would have been conspicuous from the bio-optical sensors on the float
661 (see Figure 10). Such a constant and low export flux may have been driven by self-regulation
662 of the thickness and integrated Chl (a community response analogous to the cellular self-
663 shading 'package effect') within the DCM (see Lande et al., 1989). As stated earlier, the
664 ability of large polar diatoms to increase their light-harvesting antennae (a mechanism that
665 requires no additional Fe, Strzepek et al., 2012, 2019) may have exacerbated this Chl
666 'package' effect leading to their vertical export. There is some evidence of such a low but

667 constant export flux from Chl fluorescence and backscatter from January to April 2021
668 (Figure 10). However, these downward fluxes are more evident for backscatter than for Chl
669 fluorescence suggesting chlorotic cells with declining Chl relative to carbon. Such chlorotic
670 cells would be linked to their senescence after less than a week (Strzepek et al., 2012), based
671 on observations of lab-cultured S. Ocean polar diatoms under high Fe but low light
672 conditions (i.e., reflecting the environment within the DCM/DBM). These observations help
673 inform on the wider functional role of the DCM and DBM.
674
675 *4.5 Ecological and biogeochemical roles of the DCM/DBM*
676 Recent reviews of S. Ocean NPP (Pinkerton et al., 2021) and biogeochemistry (Henley et al.,
677 2021) suggest DCMs play important ecological and/or biogeochemical roles based on particle
678 export. Our suite of datasets from diverse observational platforms offers insights into the
679 wider roles of DCMs/DBMs. The co-location of both the DCM and DBM, which is mainly
680 associated with diatoms, along with its multi-month persistence suggests that it is a
681 subsurface niche that develops as a result of the decline of the surface mixed layer
682 phytoplankton community (S-Figure 4 and S-Table 1) following resource limitation by both
683 silicate and Fe. The surface waters appear, based on the BGC-ARGO float records (Figure 9),
684 to have low and constant Chl and C concentrations, that characterise a seasonal High-Nutrient
685 Low-Chlorophyll province (Boyd et al., 2000; Boyd and Law 2001; Arrigo et al., 2003). The
686 development of the subsurface diatom community will have ramifications for the cycles of Fe,
687 silicate and C in particular. The diatom community appears to be driven by the availability of
688 silicate below the seasonal mixed layer along with Fe derived from recycling rather than new
689 sources. NPP is relatively low – we measured 0.2 μmol L^{-1} d^{-1} in the DCM. Other studies
690 have estimated NPP from DCMs, but these are based on snapshots from short station
691 occupations. Parslow et al. (2001) reported a maximum rate of NPP of 0.25 μmol L^{-1} d^{-1}

692 (equivalent to the daily 'production' of 4 x 10^4 (*E. antarctica*) to 5.5 x 10^4 (*P. inermis*)
693 diatom cells L^{-1} (based on S-materials in Strzepek et al., 2019) in the DCM in October and
694 January, decreasing to <0.1 μmol L^{-1} d^{-1} in March.
695
696 Prior NPP estimates (Parslow et al., 2001) did not take into consideration the thickness of the
697 stratum associated with the DCM/DBM. Based on robust estimates, from our three
698 observational approaches, we can extrapolate this NPP rate over the ~25 m thick feature
699 (Figure 9) resulting in a column integral of 5.0 mmol m^{-2} d^{-1}. Further extrapolation, based on
700 little change in C:Chl ratios which is indicative of relatively healthy cells, to a month
701 suggests that an NPP of 150 mmol m^{-2} monthly could be contributed by this feature which
702 persisted for 3 months (Figure 9). The fate of this additional carbon is unknown, but based on
703 the bio-optical sensor time-series (Figure 10), could be a 'slow trickle' of exported particles
704 to depth. Herbivory data during the ship occupation of the 56°S site suggest that salps can
705 ingest but not consume these large diatoms (S-Figure 7). Thus, it is possible that most losses
706 can be attributed to export rather than secondary consumption, leading to a 'slow trickle' of
707 up to 150 mmol POC m^{-2} each month from ~ 90 m depth.
708
709 Is there a biogeographic province for S. Ocean DCM/DBMs? Our findings, along with those
710 from Parslow et al. (2001) south of Australia, and several of the floats featured in the Cornec
711 et al. (2021a) global DCM analysis, but re-examined in detail here (Figure 11), suggest that
712 the IPFZ may be such a region. This region can provide both silicate at depth and *in situ* Fe
713 recycling by microbes associated with the subsurface ammonium maximum. However,
714 additional insights come from observations from the waters north and south of the IPFZ. To
715 the north, in the subantarctic, which also has seasonal silicate limitation (Hutchins et al.,
716 2001), there is no evidence of DCM or DBM, suggesting that alleviation of similar limitation

717 at depth alone may not result in a DCM/DBM. To the south of the IPFZ, the SOIREE site
718 (Trull et al., 2001) was south of the southern branch of the Polar Front, in eastward flowing
719 Antarctic Circumpolar Current waters. This site was characterized by a Tmin layer (but there
720 are no ammonium data), and Figure 9 in Trull et al. (2001) reveals that silicate most likely is
721 never fully depleted in surface waters at 61°S. Thus, the physico-chemical characteristics of
722 the IPFZ may play a key role by being both silicate and Fe deplete in surface waters, yet
723 being able to provide both nutrients in the subsurface, but via different mechanisms – from
724 the nutricline for silicate and via recycling for Fe. The IPFZ thus provides an interesting
725 testbed to see if it represents a province in which both DCM and DBM are co-located, as
726 opposed to other regions where only DCMs comprising photoacclimated cells are evident
727 (Carranza et al., 2018; Baldry et al., 2021; Cornec et al., 2021a).
728
729 Acknowledgments
730 Many thanks to the scientific staff and crew of the RV Investigator who safely and
731 successfully navigated us around the three SOLACE sites in the Southern Ocean.
732
733
734
735
736
737
738
739 References
740 Argo (2000). Argo float data and metadata from Global Data Assembly Centre (Argo GDAC).
741 SEANOE. https://doi.org/10.17882/42182
742 Allen, J. T., Brown, L., Sanders, R., Moore, C. M., Mustard, A., Fielding, S., et al. (2005).
743 Diatom carbon export enhanced by silicate upwelling in the northeast Atlantic. Nature,
744 437(7059), 728–732. https://doi.org/10.1038/nature03948

745 Arrigo, K. R., van Dijken, G. L., and Bushinsky, S. (2008). Primary production in the
746 Southern Ocean, 1997–2006. J. Geophys. Res. Oceans 113:C08004.

747 Arrigo, K. R., van Dijken, G. L., and Strong, A. L. (2015). Environmental controls of marine
748 productivity hot spots around Antarctica. J. Geophys. Res. Oceans 120, 5545–5565. doi:
749 10.1002/2015JC010888

750 Baldry, K., Strutton, P. G., Hill, N. A., & Boyd, P. W. (2020). Subsurface Chlorophyll-a
751 Maxima in the Southern Ocean. Frontiers in Marine Science, 7, 671.
752 https://doi.org/10.3389/fmars.2020.00671

753 Barbieux, M., Uitz, J., Gentili, B., Pasqueron De Fommervault, O., Mignot, A., Poteau, A., et
754 al. (2019). Bio-optical characterization of subsurface chlorophyll maxima in the
755 Mediterranean Sea from a Biogeochemical-Argo float database. Biogeosciences, 16(6),
756 1321–1342. https://doi.org/10.5194/bg-16-1321-2019

757 Behrenfeld, M. J., Boss, E., Siegel, D. A. & Shea, D. M. Carbon-based ocean productivity
758 and phytoplankton physiology from space. Glob. Biogeochem. Cycles 19, GB1006 (2005)

759 Bock N, Subramaniam A, Juhl AR, Montoya J and Duhamel S (2022) Quantifying Per-Cell
760 Chlorophyll a in Natural Picophytoplankton Populations Using FluorescenceActivated Cell
761 Sorting. Front. Mar. Sci. 9:850646. doi: 10.3389/fmars.2022.850646

762 Boyd, P. W., Watson, A. J., Law, C. S., Abraham, E. R., Trull, T., Murdoch, R., et al. (2000).
763 A mesoscale phytoplankton bloom in the polar Southern Ocean stimulated by iron
764 fertilization. Nature 407, 695–702. doi: 10.1038/35037500

765 Boyd P.W. and C.S Law 2001 The Southern Ocean Iron Release Experiment (SOIREE)—
766 introduction and summary. Deep-SeaRes II, 48, 2425–2438.

767 Boyd, P. W., and E. R. Abraham. 2001. Iron-mediated changes in phytoplankton
768 photosynthetic competence during SOIREE. Deep-Sea Res. (II Top. Stud. Oceanogr.) 48:
769 2529. doi:10.1016/s0967-0645(01)00007-8

770 Boyd P.W., S.C. Doney, $S._{Eggins}$, M.J. Ellwood, M. Fourquez, B.L. Nunn, R.F. Strzepek, E.
771 Timmins-Schiffman (2022). Transitioning global change experiments on Southern Ocean
772 phytoplankton from lab to field settings: Insights and challenges. Limnology and
773 Oceanography, 67, 1911-1930. doi: 10.1002/lno.12175
774

775 Boyer Montégut, C. de., G. Madec, A.S. Fischer, A. Lazar, and D. Iudicone (2004) Mixed
776 layer depth over the global ocean: An examination of profile data and a profile-based
777 climatology. Journal of Geophysical Research: Oceans, 109, Issue C12.
778 https://doi.org/10.1029/2004JC002378

779 Briggs, N., G. Dall'Olmo and H. Claustre (2020) Major role of particle fragmentation in
780 regulating biological sequestration of CO_2 by the oceans. Science, 367(6479):791-793. doi:
781 10.1126/science.aay1790.

782 Carranza, M. M., Gille, S. T., Franks, P. J. S., Johnson, K. S., Pinkel, R., and Girton, J. B.
783 (2018). When Mixed Layers Are Not Mixed. Storm-Driven Mixing and Biooptical Vertical

784 Gradients in Mixed Layers of the Southern Ocean. J. Geophys. Res. Oceans 123, 7264–7289.
785 doi: 10.1029/2018JC014416

786 Cloern, J. E., Grenz, C., & Vidergar-Lucas, L. (1995). An empirical model of the
787 phytoplankton chlorophyll: Carbon ratio-the conversion factor between productivity and
788 growth rate. *Limnology & Oceanography*, *40*(7), 1313–1321.
789 https://doi.org/10.4319/lo.1995.40.7.1313

790 Cornec, M., Claustre, H., Mignot, A., Guidi, L., Lacour, L., Poteau, A., et al. (2021a). Deep
791 chlorophyll maxima in the global ocean: Occurrences, drivers and characteristics. Global
792 Biogeochemical Cycles, 35, e2020GB006759. https://doi. org/10.1029/2020GB006759

793 Cornec, M., R. Laxenaire, S. Speich, H. Claustre (2021b) Impact of Mesoscale Eddies on
794 Deep Chlorophyll Maxima. https://doi.org/10.1029/2021GL093470

795 Cullen, J. J. (1982). The deep chlorophyll maximum: Comparing vertical profiles of
796 chlorophyll a. Canadian Journal of Fisheries and Aquatic Sciences, 39(5), 791–803.
797 https://doi.org/10.1139/f82-108

798 Cullen, J. J. (2015). Subsurface chlorophyll maximum layers: Enduring enigma or mystery
799 solved? Annual Review of Marine Science, 7(1), 207–239. https://doi.org/10.1146/annurev-
800 marine-010213-135111

801 Cullen, J. J., & Eppley, R. (1981). Chlorophyll maximum layers of the southern-california
802 bight and possible mechanisms of their formation and maintenance. Oceanologica Acta, 4(1),
803 23–32.

804 Dong, S., S.T. Gille and J. Sprintall et al, (2007), An Assessment of the Southern Ocean
805 Mixed Layer Heat Budget. Journal of Climate. DOI: 10.1175/JCLI4259.1

806 Ellwood, M.J., Strzepek, R., Chen, X., Trull, T.W., Boyd, P.W. (2020b). Some observations
807 on the biogeochemical cycling of zinc in the Australian sector of the Southern Ocean: a
808 dedication to Keith Hunter. Marine and Freshwater Research 71, 355-373.

809 Ellwood, M. J. et al. (2020a) Distinct iron cycling in a Southern Ocean eddy. Nature
810 communications 11, 825, doi:10.1038/s41467-020-14464-0.

811 Henley, S., Cavan, E. L., Fawcett, S. E., Kerr, R., Monteiro, T., Sherrell, R. M., et al. (2020).
812 Changing biogeochemistry of the Southern Ocean and its ecosystem implications. Front. Mar.
813 Sci. 7:581. doi: 10.3389/fmars.2020.00581

814 Hogle, S.L., C.L. Dupont, B.M. Hopkinson, A.L. King, K.N. Buck, K.L. Roe, R.K. Stuart,
815 A.E. Allen, E.L. Mann, Z.I. Johnson, and K.A. Barbeau (2018) Pervasive iron limitation at
816 subsurface chlorophyll maxima of the California Current. PNAS,115, 13300-13305.
817 www.pnas.org/cgi/doi/10.1073/pnas.1813192115

818 Holm-Hansen, O., & Hewes, C. D. (2004). Deep chlorophyll-a maxima (DCMs) in Antarctic
819 waters: I. Relationships between DCMs and the physical, chemical, and optical conditions in
820 the upper water column. Polar Biology, 27(11), 699–710. https://doi.org/10.1007/s00300-
821 004-0641-1

822 Holm-Hansen, O., Kahru, M., & Hewes, C. D. (2005). Deep chlorophyll a maxima (DCMs)
823 in pelagic Antarctic waters. II. Relation to bathymetric features and dissolved iron
824 concentrations. Marine Ecology Progress Series, 297, 71–81.
825 https://doi.org/10.3354/meps297071

826 Holte J. and L. Talley (2009), A New Algorithm for Finding Mixed Layer Depths with
827 Applications to Argo Data and Subantarctic Mode Water Formation. Journal of Atmospheric
828 and Oceanic Technology. DOI: 10.1175/2009JTECHO543.1

829 Hopkinson, B. M., & Barbeau, K. A. (2008). Interactive influences of iron and light
830 limitation on phytoplankton at subsurface chlorophyll maxima in the eastern North Pacific.
831 Limnology & Oceanography, 53(4), 1303–1318. https://doi.org/10.4319/lo.2008.53.4.1303

832 Hopkinson, Brian M., B. Greg Mitchell, Rick A. Reynolds, Haili Wang, Karen E. Selph,
833 Christopher I. Measures, Christopher D. Hewes, Osmund Holm-Hansen, and Katherine A.
834 Barbeau. 2007. Iron Limitation across Chlorophyll Gradients in the Southern Drake Passage:
835 Phytoplankton Responses to Iron Addition and Photosynthetic Indicators of Iron Stress.
836 Limnology and Oceanography 52 (6): 2540–54. https://doi.org/10.4319/lo.2007.52.6.2540

837 Hoppe, C.J.M. (2021) Always ready? Primary production of Arctic phytoplankton at the end
838 of the polar night. Limnology and Oceanography Letters 7, 2022, 167–174/ doi:
839 10.1002/lol2.10222

840 Hutchins, D. A., Crossley, A. C., DiTullio, G. R., Griffiths, F. B., Boyd, P. W., Queguiner, B.,
841 et al. (2001). Control of phytoplankton growth by iron and silicic acid availability in the
842 Subantarctic Southern Ocean: Experimental results from the SAZ project. Journal of
843 Geophysical Research, 106(2000), 31,573. https://doi.org/10.1029/2000JC000348

844 Huang, J., & Xu, F. (2018). Observational Evidence of Subsurface Chlorophyll Response to
845 Mesoscale Eddies in the North Pacific. Geophysical Research Letters, 45(16), 8462–8470.
846 https://doi.org/10.1029/2018gl078408

847 Gomi, Y., Fukuchi, M., & Taniguchi, A. (2010). Diatom assemblages at subsurface
848 chlorophyll maximum layer in the eastern Indian sector of the Southern Ocean in summer.
849 Journal of Plankton Research, 32(7), 1039–1050. https://doi.org/10.1093/plankt/fbq031

850 Johnson, R., P. G. Strutton, S. W. Wright, A. McMinn, and K. M. Meiners (2013), Three
851 improved Satellite Chlorophyll algorithms for the Southern Ocean, J. Geophys. Res. Oceans,
852 118, 3694–3703, doi:10.1002/jgrc.20270.

853 Kemp, A. E. S., Pike, J., Pearce, R. B., & Lange, C. B. (2000). The "Fall dump" – A new
854 perspective on the role of a "shade flora" in the annual cycle of diatom production and export
855 flux. Deep-Sea Research Part II: Topical Studies in Oceanography, 47(9–11), 2129–2154.
856 https://doi.org/10.1016/s0967-0645(00)00019-9

857 Kiefer, D., Olson, R. J., & Holm-Hansen, O. (1976). Another look at the nitrite and
858 chlorophyll maxima in the central North Pacific. Deep-Sea Research and Oceanographic
859 Abstracts, 23(12), 1199–1208. https://doi.org/10.1016/0011-7471(76)90895-0

860 Kennedy, F., A. Martin, J. P. Bowman, R. Wilson, and A. McMinn. 2019. Dark metabolism:
861 A molecular insight into how the Antarctic sea-ice diatom Fragilariopsis cylindrus survives
862 long-term darkness. New Phytol. 223: 675–691. doi:10.1111/nph.15843

Kopczynska, E.E., F. Dehairs, M. Elskens and S. Wright (2001) Phytoplankton and microzooplankton variability between the Subtropical and Polar Fronts south of Australia: Thriving under regenerative and new production in late summer. JGR Oceans, https://doi.org/10.1029/2000JC000278

Klunder, M. B., Laan, P., Middag, R., De Baar, H. J., & van Ooijen, J. C. (2011). Dissolved iron in the Southern Ocean (Atlantic sector). *Deep-Sea Research Part II: Topical Studies in Oceanography*, *58*(25–26), 2678–2694. https://doi.org/10.1016/j.dsr2.2010.10.042

Kwong LE; Henschke N; Pakhomov EA; Everett JD; Suthers IM, 2020, 'Mesozooplankton and Micronekton Active Carbon Transport in Contrasting Eddies', Frontiers in Marine Science, vol. 6, http://dx.doi.org/10.3389/fmars.2019.00825

Latour, P., Eggins, S., van der Merwe, P., Bach, L. T., Boyd, P. W., Ellwood, M. J., Bowie, A. R., Wuttig, K., Pinfold, T. L and R. F. Strzepek, *in prep*. 'Characterization of a Southern Ocean deep chlorophyll maximum: response of phytoplankton to light, iron and manganese enrichment.

Lande, R., W.K. Li, E.P.W. Horne and M. Wood (1989) Phytoplankton growth rates estimated from depth profiles of cell concentration and turbulent diffusion. Deep-Sea Research, 36, 1141-1159.

Latour, P., Eggins, S., van der Merwe, P., Bach, L., Boyd, P.W., Ellwood, M., Bowie, A., Wuttig, K., and R. Strzepek (submitted) Characterization of a Southern Ocean deep chlorophyll maximum: response of phytoplankton to light, iron and manganese enrichment. Limnology and Oceanography Letters

Marañón, E., F. Van Wambeke, J. Uitz, E.S. Boss, C. Dimier, J. Dinasquet, A. Engel, N Haëntjens, M. Pérez-Lorenzo, V. Taillandier, and B. Zäncker (2021) Deep maxima of phytoplankton biomass, primary production and bacterial production in the Mediterranean Sea. Biogeosciences, 18, 1749–1767, 2021 https://doi.org/10.5194/bg-18-1749-2021

Moeller, H.V., C. Laufkötter, E.M. Sweeney & M.D. Johnson (2019) Light-dependent grazing can drive formation and deepening of deep chlorophyll maxima.Nature Communications volume 10, Article number: 1978.

Mdutyana, M., Thomalla, S. J., Philibert, R., Ward, B. B., & Fawcett, S. E. (2020). The seasonal cycle of nitrogen uptake and nitrification in the Atlantic sector of the Southern Ocean. Global Biogeochemical Cycles, 34, e2019GB006363. https://doi.org/10.1029/2019GB006363

Meyerink, S.W., Ellwood, M.J., Maher, W.A., Dean Price, G., Strzepek, R.F., 2017. Effects of iron limitation on silicon uptake kinetics and elemental stoichiometry in two Southern Ocean diatoms, Eucampia antarctica and Proboscia inermis, and the temperate diatom Thalassiosira pseudonana. Limnol. Oceanogr. 62, 2445–2462.

Nelson D.M., M.A. Brzezinski, D.E. Sigmon, and V. M. Frank 2001. A seasonal progression of Si limitation in the Pacific sector of the Southern Ocean. Deep-Sea Res. II 48:3973–3995.

902 Paasche, E. 1973. Silicon and the Ecology of Marine Plankton Diatoms. I. Thalassiosira
903 Pseudonana (Cyclotella Nana) Grown in a Chemostat with Silicate as Limiting Nutrient.
904 *Marine Biology* 19 (2): 117–26. https://doi.org/10.1007/BF00353582.

905 Parslow, J. S., Boyd, P. W., Rintoul, S. R., & Griffiths, F. B. (2001). A persistent subsurface
906 chlorophyll maximum in the Interpolar Frontal Zone south of Australia: Seasonal progression
907 and implications for phytoplankton-light-nutrient interactions. Journal of Geophysical
908 Research, 106(C12), 31543–31557. https://doi.org/10.1029/2000jc000322

909 Pinkerton MH, Boyd PW, Deppeler S, Hayward A, Höfer J and Moreau S (2021) Evidence
910 for the Impact of Climate Change on Primary Producers in the Southern Ocean. Front. Ecol.
911 Evol. 9:592027. doi: 10.3389/fevo.2021.592027

912 Pollehne F., B. Klein, and B. Zeitzschel (1993) Low light adaptation and export production in
913 the deep chlorophyll maximum layer in the northern Indian Ocean, Deep Sea Research Part II:
914 Topical Studies in Oceanography, Volume 40, 737-752, https://doi.org/10.1016/0967-
915 0645(93)90055-R.

916 Queguiner, B. (2013). "Iron fertilization and the structure of planktonic communities in high
917 nutrient regions of the Southern Ocean." Deep Sea Research Part II: Topical Studies in
918 Oceanography 90: 43-54.

919 Quéguiner, B. (2001). Biogenic silica production in the Australian sector of the Subantarctic
920 Zone of the Southern Ocean in late summer 1998. Journal of Geophysical Research,
921 106(C12), 31627–31636. https://doi.org/10.1029/2000jc000249

922 Rees, C., Pender, L., Sherrin, K., Schwanger, C., Hughes, P., Tibben, S., Marouchos, A. and
923 M. Rayner. 2018. "Methods for Reproducible Shipboard SFA Nutrient Measurement Using
924 RMNS and Automated Data Processing." *Limnology and Oceanography: Methods*,
925 December, lom3.10294. https://doi.org/10.1002/lom3.10294.

926 Riemann, B., Simonsen, P., and Stensgaard, L. (1989). The carbon and chlorophyll content of
927 phytoplankton from various nutrient regimes. J. Plankton Res. 11, 1037–1045. doi:
928 10.1093/plankt/11.5.1037

929 Schmechtig C., Claustre H., Poteau A., D'Ortenzio F. (2014). Bio-Argo quality control
930 manual for the Chlorophyll-A concentration. http://doi.org/10.13155/35385

931 Schmechtig C., Boss E. Briggs N., Claustre H. Dall'Olmo G. Poteau A. (2019). BGC Argo
932 quality control manual for particles backscattering. https://doi.org/10.13155/60262

933 Sigmon, D.E., Nelson, D.M., Brzezinski, M.A., 2002. The Si cycle in the Pacific sector of the
934 Southern Ocean: seasonal diatom production in the surface layer and export to the deep sea.
935 Deep Sea Res. Pt II 49, 1747-1763.

936 Smetacek, V. A watery arms race. *Nature* **411**, 745 (2001). https://doi.org/10.1038/35081210

937 Strutton, P. G., Trull, T. W., Phillips, H. E., Duran, E. R., & Pump, S. (2023).
938 Biogeochemical Argo floats reveal the evolution of subsurface chlorophyll and particulate
939 organic carbon in southeast Indian Ocean eddies. Journal of Geophysical Research: Oceans,
940 128, e2022JC018984. https://doi. org/10.1029/2022JC018984

941 Strzepek RF, KA Hunter, RD Frew, PJ Harrison, PW Boyd, Iron–light interactions differ in
942 Southern Ocean phytoplankton. Limnol Oceanogr 57, 1182–1200 (2012).

943 Strzepek RF, MT Maldonado, KA Hunter, RD Frew, PW Boyd, Adaptive strategies by
944 Southern Ocean phytoplankton to lessen iron limitation: Uptake of organically complexed
945 iron and reduced cellular iron requirements. Limnol Oceanogr 56, 1983–2002 (2011).

946 Strzepek, R. F., Boyd, P. W., and Sunda, W. G. (2019). Photosynthetic adaptation to low iron,
947 light, and temperature in Southern Ocean phytoplankton. Proc. Natl. Acad. Sci. U.S.A. 116,
948 4388–4393. doi: 10.1073/pnas.1810886116

949 Taylor, A. H., Geider, R. J., & Gilbert, F. J. H. (1997). Seasonal and latitudinal dependencies
950 of phytoplankton carbon-to-chlorophyll a ratios: Results of a modeling study. Marine
951 Ecology Progress Series, 152(1–3), 51–66. https://doi.org/10.3354/meps152051

952 Tripathy, S. C., Pavithran, S., Sabu, P., Pillai, H. U. K., Dessai, D. R. G., & Anilkumar, N.
953 (2015). Deep chlorophyll maximum and primary productivity in Indian Ocean sector of the
954 Southern Ocean: Case study in the Subtropical and Polar Front during austral summer 2011.
955 Deep-Sea Research Part II: Topical Studies in Oceanography, 118, 240–249.
956 https://doi.org/10.1016/j.dsr2.2015.01.004

957 Trull TW, Passmore A, Davies DM, Smit T, Berry K, Tilbrook B. Distribution of planktonic
958 biogenic carbonate organisms in the Southern Ocean south of Australia: a baseline for ocean
959 acidification impact assessment. Biogeosciences. 2018 Jan 3;15(1):31-49.

960 Uchida T., D. Balwada, R.P. Abernathey, G.A. McKinley, S.K. Smith, M. Lévy (2020)
961 Vertical eddy iron fluxes support primary production in the open Southern Ocean. Nat Comm.
962 https://doi.org/10.1038/s41467-020-14955-0

963 Westwood, K. J., Griffiths, F. B., Webb, J. P., & Wright, S. W. (2011). Primary production in
964 the Sub-Antarctic and Polar Frontal Zones south of Tasmania, Australia; SAZ-Sense survey.
965 Deep-Sea Research Part II: Topical Studies in Oceanography, 58(21–22), 2162–2178.
966 https://doi.org/10.1016/j.dsr2.2011.05.017

967 Wong, A., R. Keeley, T. Carval, and the Argo Data Management Team (2023). Argo Quality
968 Control Manual for CTD and Trajectory Data. http://dx.doi.org/10.13155/33951

969 Yool, A., & Tyrrell, T. (2003). Role of diatoms in regulating the ocean's silicon cycle. Global
970 Biogeochemical Cycles, 17(4). https://doi.org/10.1029/2002gb002018

971

972

973

974

975

976

977

Figure captions

Figure 1 Vertical profiles for the 56°S station from calibrated CTD sensors. a. temperature, b. salinity, c. irradiance (PAR), d. Chl fluorescence, e. transmissometer POC, f. POC:Chl ratio, g) proportion of detrital fraction. MLD denotes the mean Mixed Layer Depth for all profiles with +/- 1 standard deviation. Dashed lines labelled DCM and DBM denote the mean position of these subsurface features. Dotted lines in d. and e. denote the mean vertical extent of each feature. In Figure 1d. and e. the location of each subsurface feature is identified by smoothing each profile with a 10 m moving mean then identifying the maximum. The maximum is 10% larger than the mixed layer mean value to qualify. The vertical extent of each feature is defined as the region with 50% of the difference between the MLD mean and maximum concentration. Days since arriving the 56°S station on 24 December 2020, for each profile are denoted on the color bar.

Figure 2 Vertical profiles for the 56°S station from CTD rosette water samples. Dissolved Fe samples were sampled from the trace metal clean rosette. a. dissolved Fe (dFe), b. nitrate, c. ammonium, d. nitrite, e. silicate, f. phosphate, g. extracted Chl, h. biogenic silica, i. F_v/F_m, j. σ_{PSII}, k. community carbon fixation and l. community iron uptake. MLD and color bar are as for Figure 1.

Figure 3 Size- partitioned C and Fe uptake rates for three size classes and their sum (all sizes) at 56°S (solid lines 20 December 2020; dashed lines 26 December 2020) and 58°S (solid lines 29 December 2020, dashed lines 7 January 2021).

Figure 4 Vertical profiles for the 58°S station from calibrated CTD sensors. Panels are as for Figure 1, as is the MLD definition and the color bar. Arrival on station (day 0) was 1 January 2021) Note, no DCM or DBM was located using our algorithm (see Methods) at 58°S.

Figure 5 Vertical profiles for the 58°S station from and CTD rosette water samples. Dissolved Fe samples were sampled from the trace metal clean rosette. Panels are as for Figure 2 and MLD and color bar are as for Figure 3.

Figure 6 Triaxus towbody sections in the vicinity of the 56°S station (see S-Figure 4 for towbody maps that relate to the direction of the tow presented above the panels for Chl) for Chl, POC and C:Chl ratio. The red vertical line in each panel denotes the mixed layer depth.

The DCM and DBM peak (i.e., maximum concentration) and vertical extent are calculated as per Figure 1 for each profile of the towbody and denoted with black lines.

Figure 7 Triaxus towbody sections in the vicinity of the 58°S station. As per Figure 6. Note, discontinuities in DCM/DBM time-series indicate no DCM/DBM was located using our algorithm for that profile.

Figure 8 Time-series of BGC-ARGO physical observations (semi-log plots) in the vicinity of the 56°S site. a. temperature; b. salinity; c. potential density; and d. Brunt–Väisälä frequency (i.e., buoyancy frequency). MLD denotes the seasonal mixed layer depth (white line).

Figure 9 Time-series of BGC-ARGO biological observations (semi-log plots) in the vicinity of the 56°S site. a. concentration of small fluorescing particles $chla_s$ and b. small backscattering particles bbp_l, c. POC:$chla_s$ ratio and d. algal C:$chla_s$ ratio (see Methods). MLD denotes the seasonal mixed layer depth (white line).

Figure 10 Time-series of BGC-ARGO biological observations in the vicinity of the 56°S site. a. concentration of large fluorescing particles $chla_l$. and b. large backscattering particles bbp_l. The black line denotes the seasonal mixed layer depth.

Figure 10 Time-series of BGC-ARGO biological observations in the vicinity of the 56°S site presented in Figure 9a and b, but replotted with a linear (rather than log) colormap to better assess the potential export of Chl and C into the oceans' interior. The black line denotes the seasonal mixed layer depth.

Figure 11 Indo-Pacific sectors of the S. Ocean overlaid with composite of the locations of BGC-ARGO float profiles presented in Cornec et al. (2021a). Blue small symbols denote float profiles where DCM and DBMs were observed. Green symbols represent where only DCMs (but no DBM) were recorded. Gray symbols represent where no DCMs were observed. Two floats that recorded persistent DCM features are highlighted with light blue circles at 120°E and 165°E. The two polar sites (56°S 138.5°E, 58°S 141.5°E) featured in our study are denoted by red crosses. The SR3 line (from Tasmania to E. Antarctica) along which Parslow et al. (2021) recorded DCMs, only within the IPFZ, over multiple years during WOCE and JGOFS transects is represented by a yellow dashed line. The purple and red lines denote the fronts which bound the IPFZ.

Figure 12 Time-series observations of the DCM and DBM from Cornec et al. (2021) for the two floats within the IPFZ featured in Figure 11. The sampling frequency for both floats was

every 2 days before March 2017, 4 days during March 2017, and 5 days after March 2017. The mixed layer depth is denoted with a white line.

S-Figures

S-Figure 1 Locations of stations occupied during the 2020/21 SOLACE voyage (IN2020_V08) south of Tasmania, Australia. The left hand panel shows the locations of all three sites and locations of the Triaxus undulating towbody tows, superimposed on the voyage track. The right hand panel features only the polar 1 (56°S) and 2 (58°S) sites overlaid on a map of ocean color Chl and sea surface height (SSH) anomaly from early January 2021 (courtesy of Benoit Legresy, CSIRO, Australia). The two sites were located in low flow regions with low and intermediate Chl concentrations, respectively.

S-Figure 2 Location of a) the BGC-ARGO float relative to the 56°S site (red circle) from its launch in Dec 2020 to June 2021 (solid symbols, just N of 54S, W of 140E). B) drift trajectory (miles) of holey-sock drogue at 56°S polar site (denoted by red circle). Examples of Triaxus towbody routes at c) 56°S and d) 58°S.

S-Figure 3 Overview of SOLACE DCM large diatom species based on a photomicrograph using a 20-fold concentrate from the DCM at the 56S site. Species include: *Fragilariopsis kerguelensis*, *Fragilariopsis* sp. (*cylindrus/curta*), *Pseudo-nitzschia* spp., *Proboscia* sp. (*alata / inermis / truncata*), *Dactyliosolen antarctica*, *Cylindrotheca* spp., *Corethron* spp., *Chaetoceros atlanticus*, *Asteromphalus hookeri*, *Thalassiosira oliverana / tumida*.

S-Figure 4 The temporal evolution of the DCM and DBM at the 58°S site. a) Chl and d) POC profiles from Fig 3d and 3e are shown, zoomed in on upper 100 m. The associated temporal evolution of the b, e) magnitude and c, f) enhancement relative to the mean MLD concentration for the b, c) DCM and e, f) DBM are plotted. Note, the 'DBM/DCM' magnitude and enhancement are shown even if they do not technically qualify as a 'DBM/DCM' based on our threshold criteria (See Methods).

S-Figure 5 a) Depth-integrated irradiance from the BGC-ARGO float over the duration of the observed DCM/DBM. White line denotes mixed layer depth. b) Time-series of PAR at the depth of the DCM from the profiling float. Time-series of areally-averaged PAR (4 km resolution, MODIS) over period of late 2020 and early 2021 for c) 55.5°S – 56.5°S, 137.5°E – 138.5°E and d), 57.5°S-58.5°S, 140.5°E to 141.8°E.

S-Figure 6 Seasonal cycle of phytoplankton accumulation at both sites. The seasonal development of a, b) surface Chlorophyl and c, d) the depth of the SML is show for the a, c) 56°S and b, d) 58°S sites. For each, we plotted shipboard measurements (black) atop the full seasonal cycle from the a, b) remote sensing or c, d) reanalysis record (red). For the later we show the 2020-2021 cycle (solid) and the climatologic cycle (dashed). Remote sensing chlorophyll is from the MODIS-GSM ocean color record and reanalysis SML depths are from HYCOM, both downloaded from Ocean Productivity (oregonstate.edu) .. Both are averaged over the same box encompassing .5 degrees of latitude and longitude around the mean position of the occupation. Remote sensing chlorophyl is correct by a factor of 1.73 per Johnson et al. (2013).

S-Figure 7 Photomicrographs of intact diatoms within the (dissected) gut of a salp at the 58°S site suggests that diatoms are ingested but not consumed by herbivores.

S-Table 1 Phytoplankton specific growth rates in different features. Division rates are calculated by dividing NPP by phytoplankton biomass. Phytoplankton biomass is approximated with a C:Chl of 30 (g:g) in all cases except for below the surface mixed layer under the 'With Photoacclimation' assumption, where it is equal to 15 (g:g). NPP and Chlorophyl are averaged across the specified depth range for each feature, with the surface mixed layer, DBM and DCM defined as in Figures 1-4. At 58S no DCM or DBM was identified so 'Deep' value were computed over the 15 m below the surface mixed layer. NPP was averaged across all c-uptake incubation profiles (Fig. 5) and Chl was averaged across all profiles of extracted Chl (Figs. 2, 4)

Figures 1 to 12.

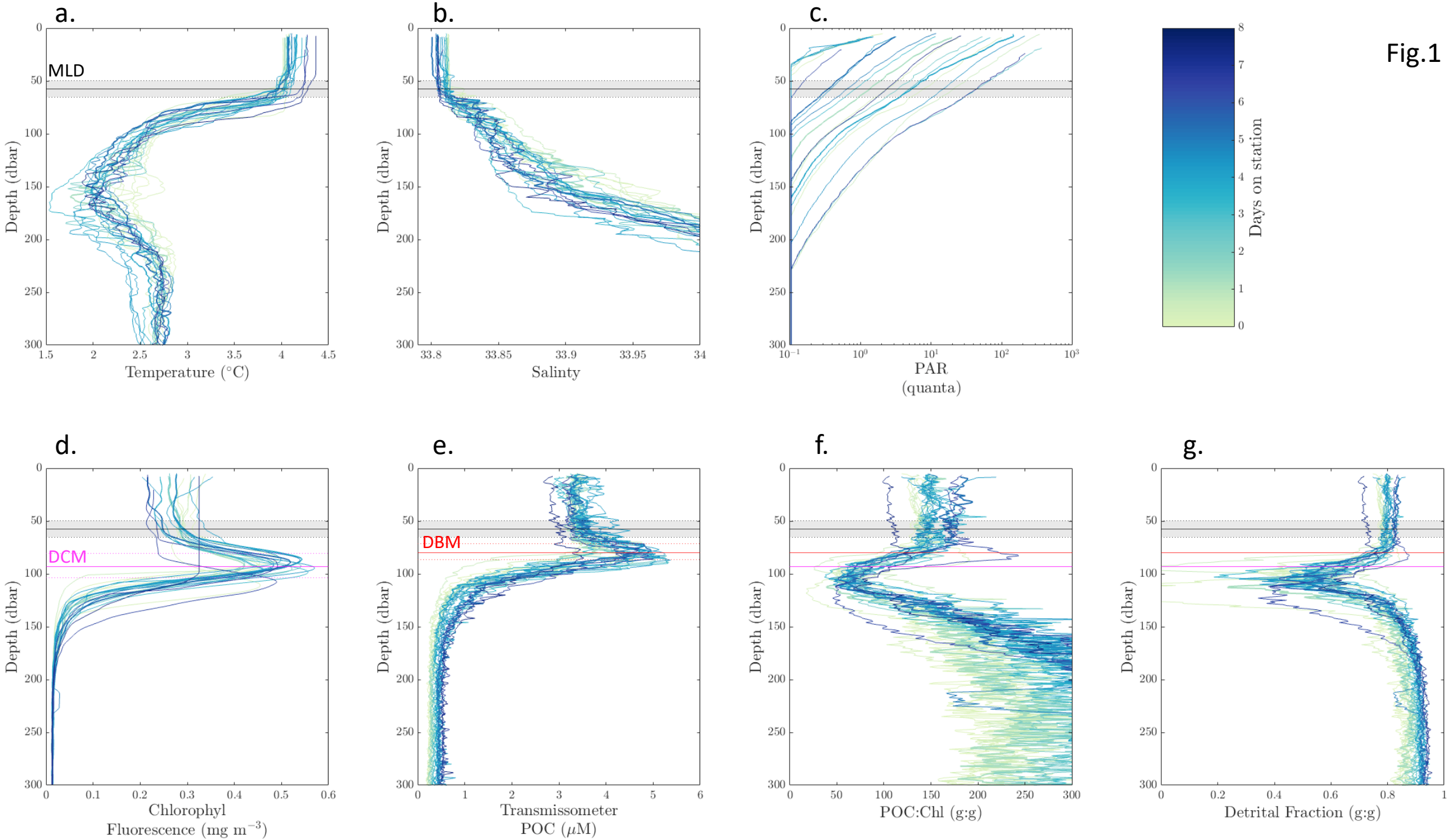
a.
MLD
Depth (dbar)
Temperature (°C)
b.
Depth (dbar)
Salinty
c.
Depth (dbar)
PAR
(quanta)
Days on station
d.
DCM
Depth (dbar)
Chlorophyl
Fluorescence (mg m^{-3})
e.
DBM
Depth (dbar)
Transmissometer
POC (μM)
f.
Depth (dbar)
POC:Chl (g:g)
g.
Depth (dbar)
Detrital Fraction (g:g)

Fig.1

Fig. 2

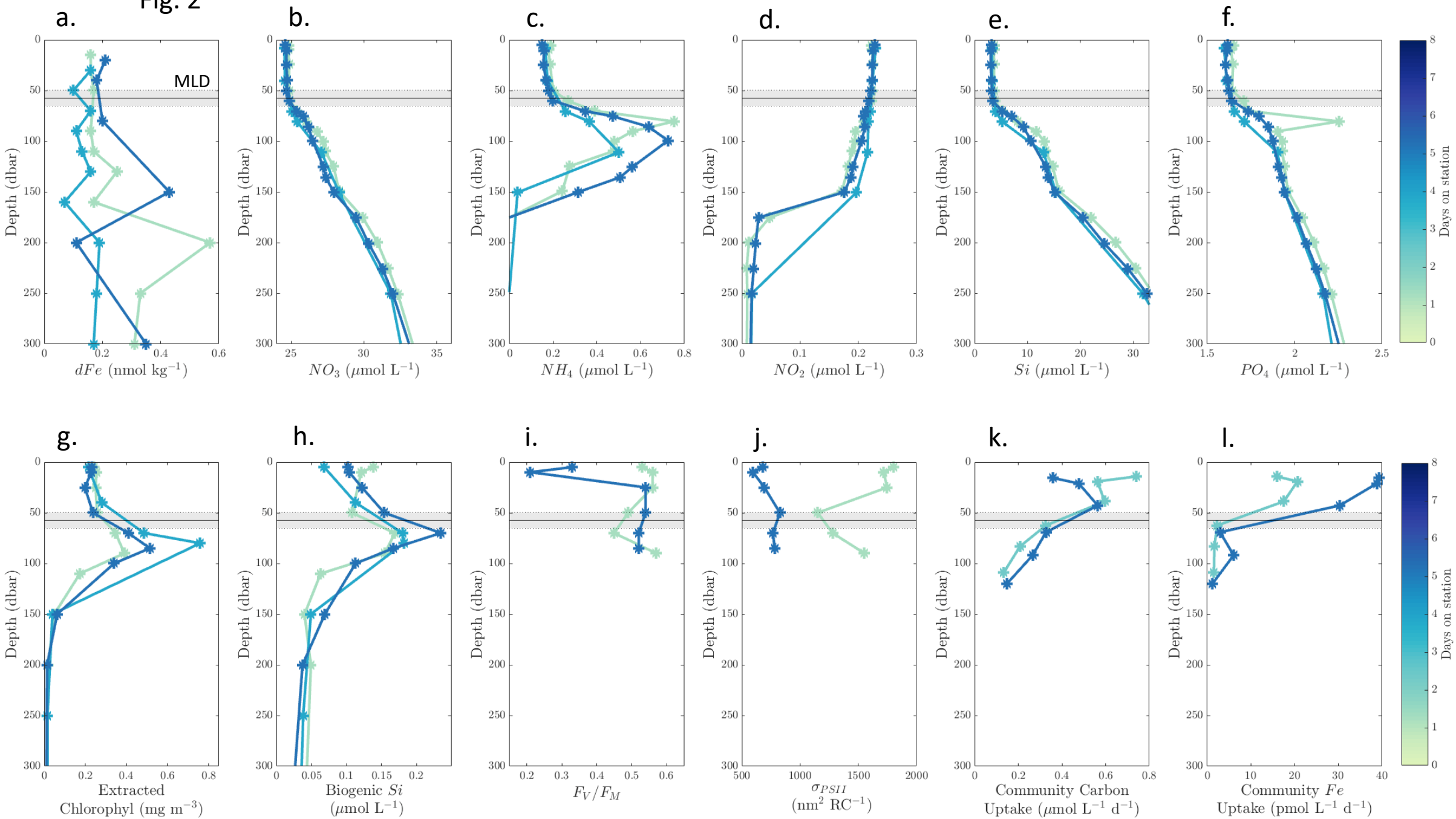
a.
b.
c.
d.
e.
f.
g.
h.
i.
j.
k.
l.
MLD
Depth (dbar)
dFe (nmol kg^{-1})
NO_3 (μmol L^{-1})
NH_4 (μmol L^{-1})
NO_2 (μmol L^{-1})
Si (μmol L^{-1})
PO_4 (μmol L^{-1})
Extracted Chlorophyl (mg m^{-3})
Biogenic Si (μmol L^{-1})
F_V/F_M
σ_{PSII} (nm^2 RC^{-1})
Community Carbon Uptake (μmol L^{-1} d^{-1})
Community Fe Uptake (pmol L^{-1} d^{-1})
Days on station

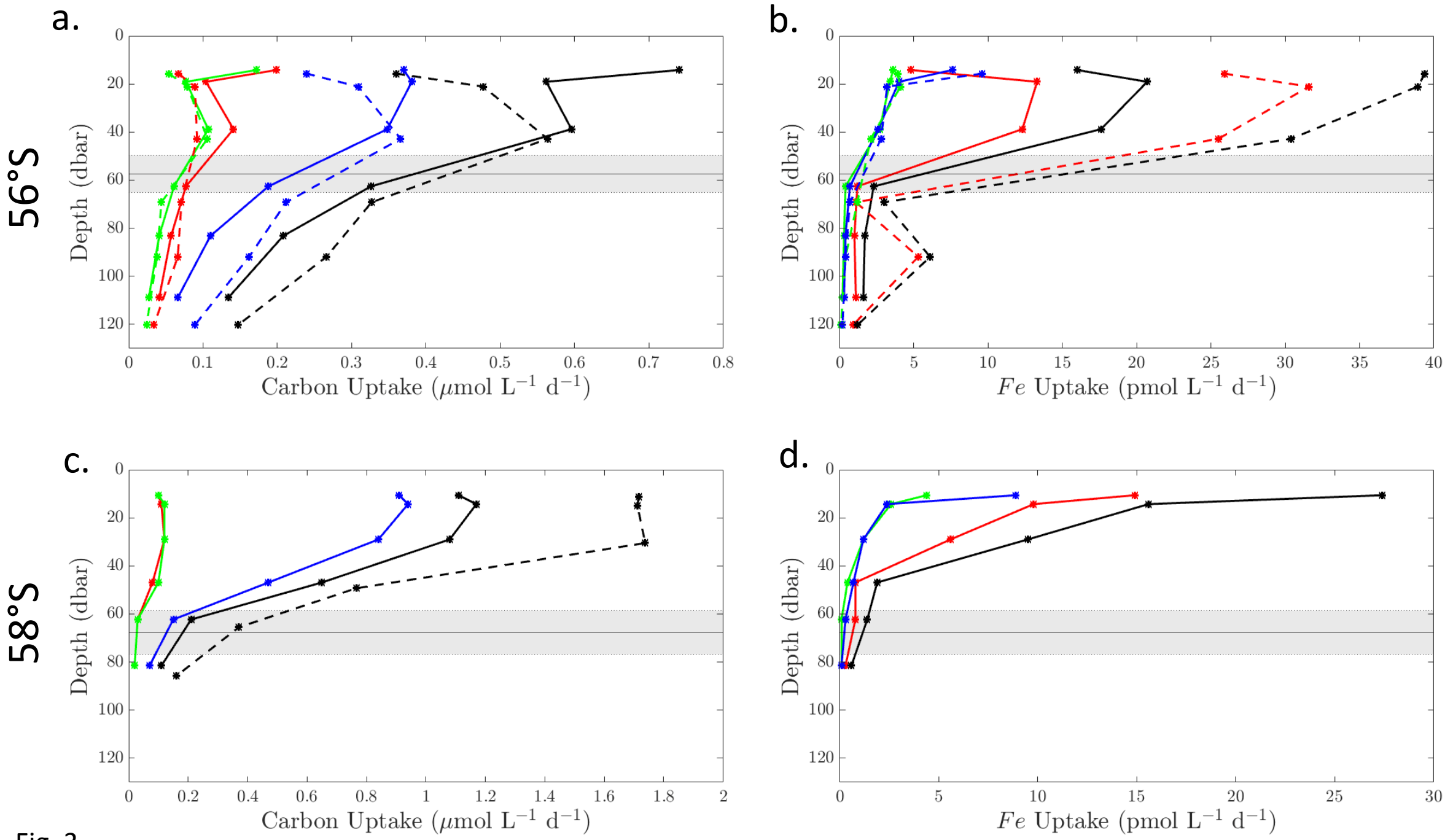
a.
b.
c.
d.
56°S
58°S
Depth (dbar)
Carbon Uptake (μmol L^{-1} d^{-1})
Fe Uptake (pmol L^{-1} d^{-1})
0.2 – 2 µm
2 – 20 µm
>20 µm
All Sizes

Fig. 3

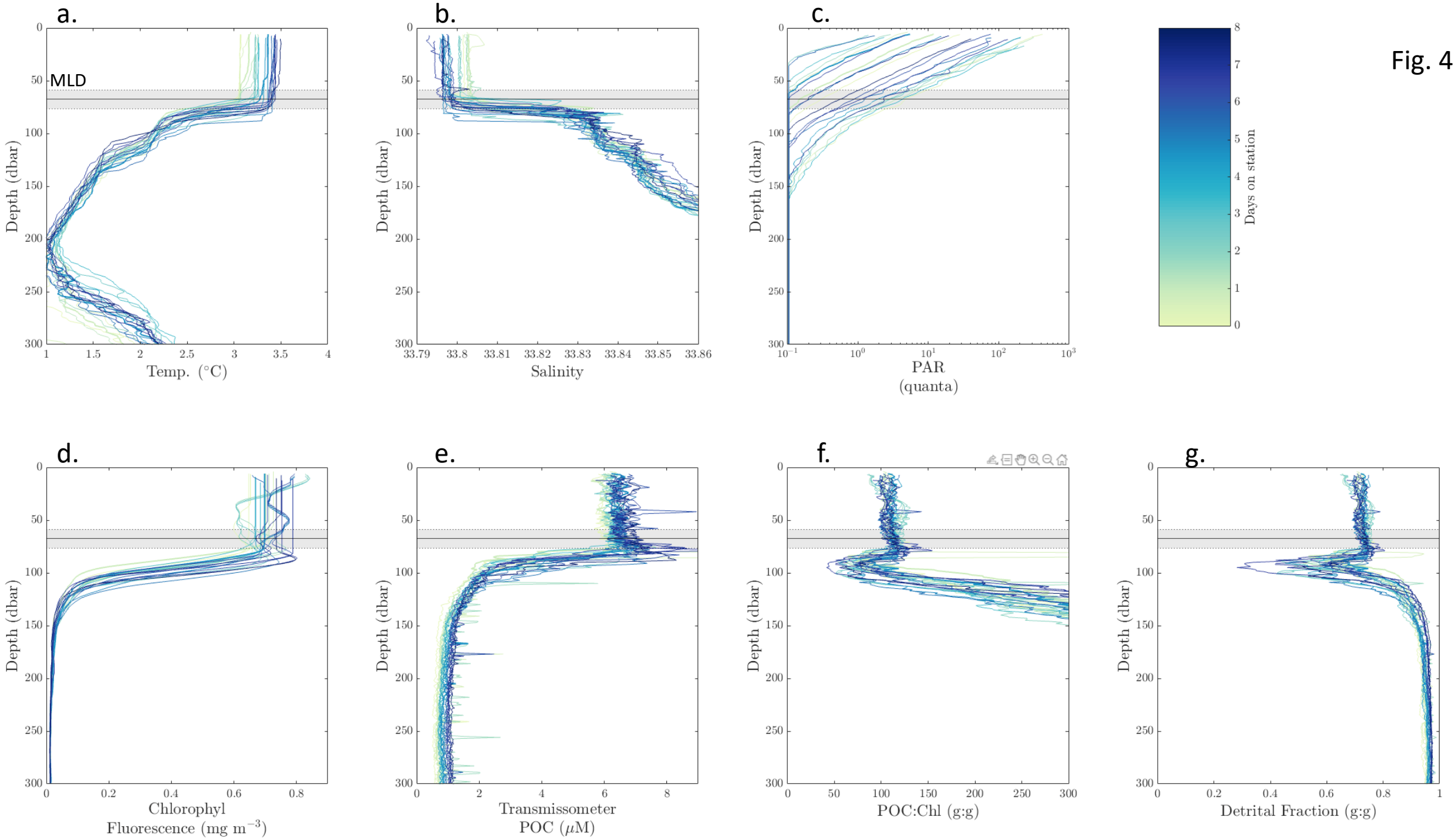
a.
MLD
Depth (dbar)
Temp. (°C)
b.
Salinity
c.
PAR
(quanta)
Days on station
d.
Chlorophyl
Fluorescence (mg m^{-3})
e.
Transmissometer
POC (μM)
f.
POC:Chl (g:g)
g.
Detrital Fraction (g:g)

Fig. 4

Fig. 5

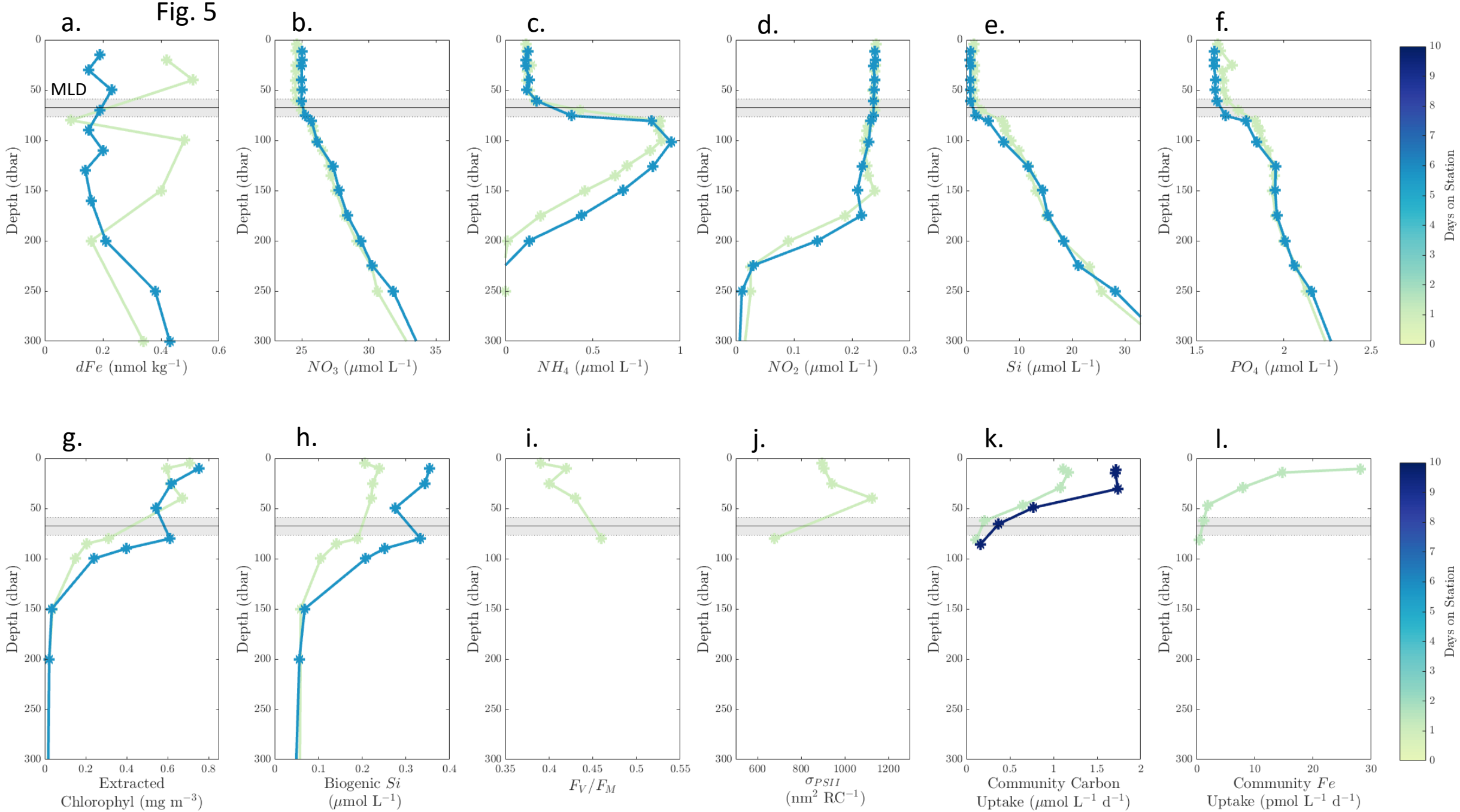
a.
b.
c.
d.
e.
f.
g.
h.
i.
j.
k.
l.
MLD
Depth (dbar)
dFe (nmol kg^{-1})
NO_3 (μmol L^{-1})
NH_4 (μmol L^{-1})
NO_2 (μmol L^{-1})
Si (μmol L^{-1})
PO_4 (μmol L^{-1})
Extracted Chlorophyl (mg m^{-3})
Biogenic Si (μmol L^{-1})
F_V/F_M
σ_{PSII} (nm^2 RC^{-1})
Community Carbon Uptake (μmol L^{-1} d^{-1})
Community Fe Uptake (pmol L^{-1} d^{-1})
Days on Station

Fig. 6

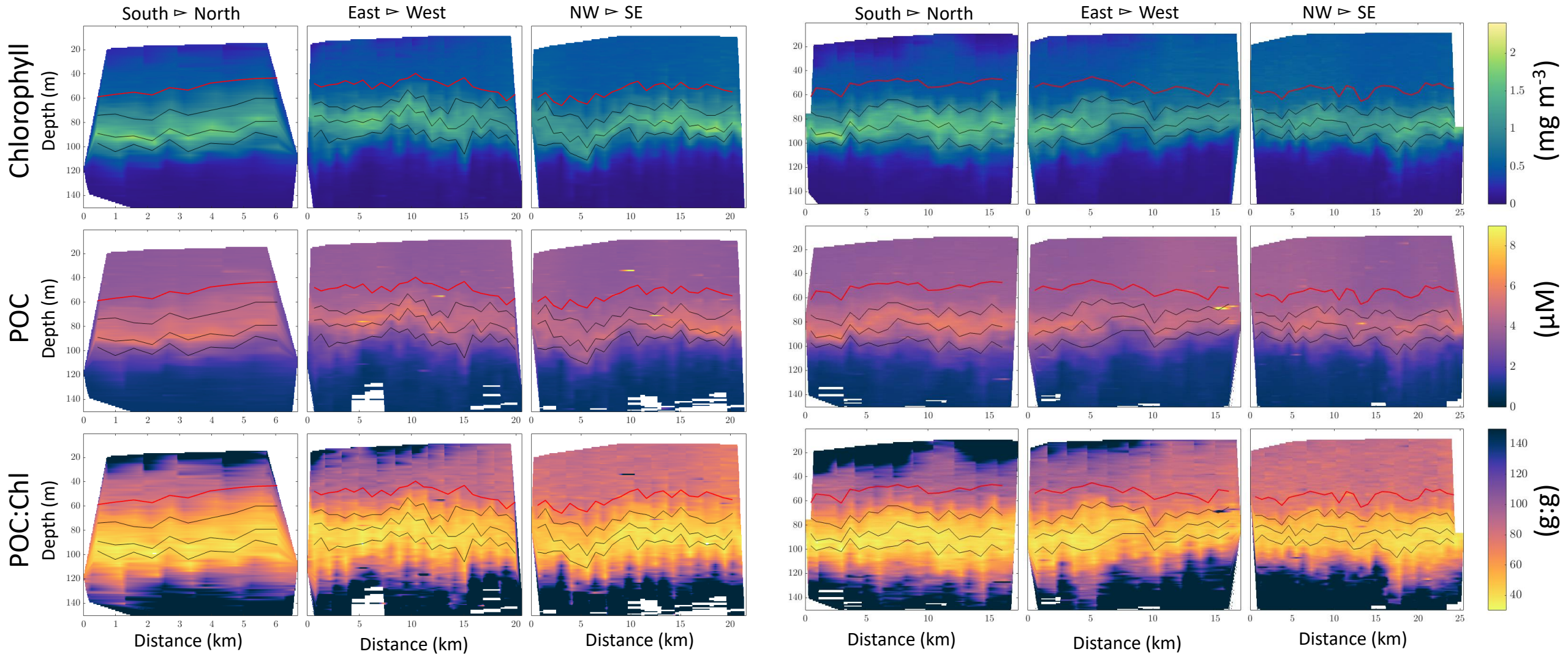
56°S: Tow 1-3: Dec 29
56°S: Tow 4-6: Dec 30
South ▻ North
East ▻ West
NW ▻ SE
Chlorophyll
POC
POC:Chl
Depth (m)
Distance (km)
(mg m-3)
(µM)
(g:g)

Fig. 7

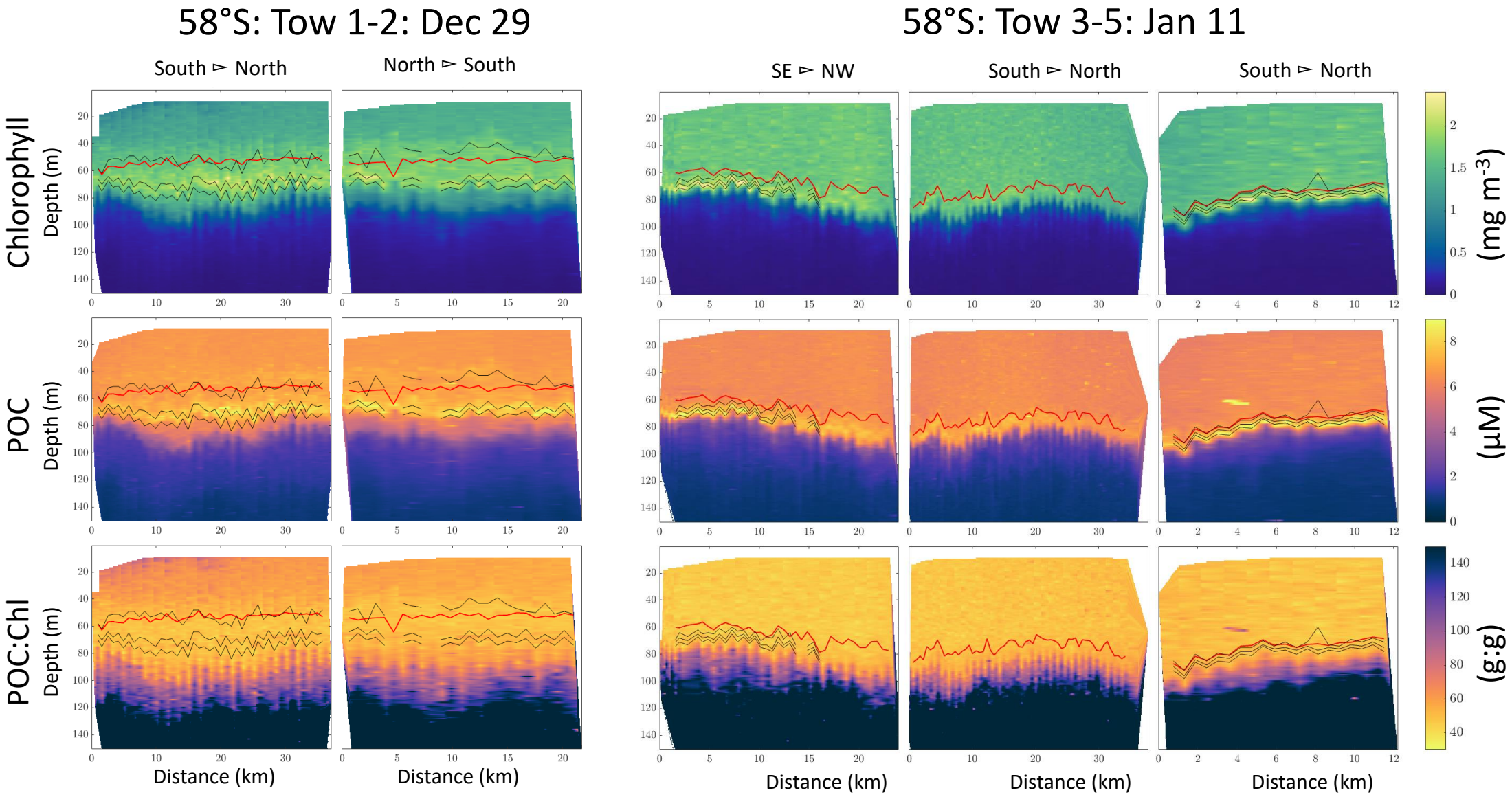
58°S: Tow 1-2: Dec 29
58°S: Tow 3-5: Jan 11
South ▻ North
North ▻ South
SE ▻ NW
South ▻ North
South ▻ North
Chlorophyll
POC
POC:Chl
Depth (m)
Distance (km)
(mg m-3)
(µM)
(g:g)

Figure 8

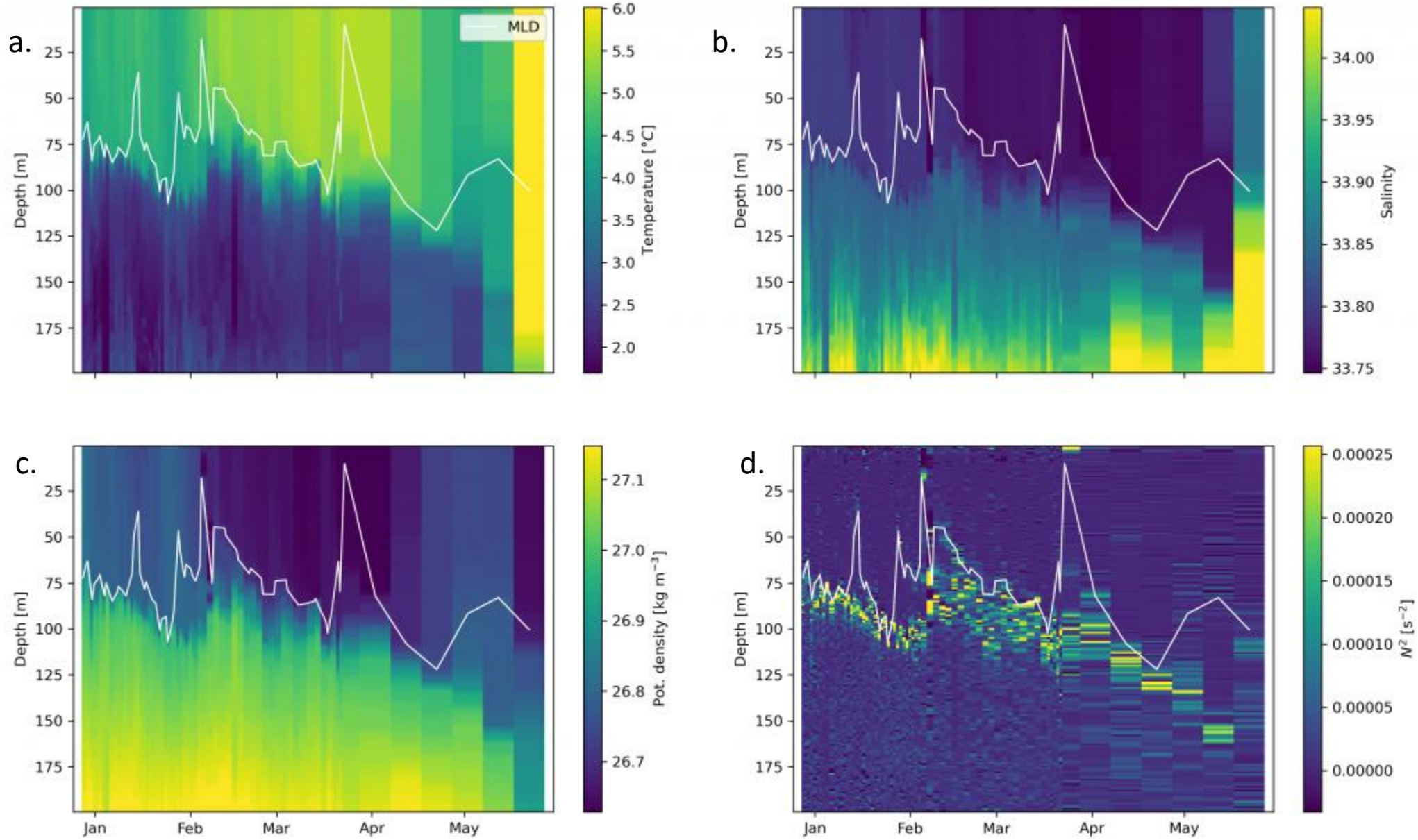
a.
MLD
Depth [m]
25
50
75
100
125
150
175
6.0
5.5
5.0
4.5
4.0
3.5
3.0
2.5
2.0
Temperature [°C]
b.
Depth [m]
34.00
33.95
33.90
33.85
33.80
33.75
Salinity
c.
Depth [m]
27.1
27.0
26.9
26.8
26.7
Pot. density [kg m^{-3}]
Jan
Feb
Mar
Apr
May
d.
Depth [m]
0.00025
0.00020
0.00015
0.00010
0.00005
0.00000
N^2 [s^{-2}]
Jan
Feb
Mar
Apr
May

Figure 9

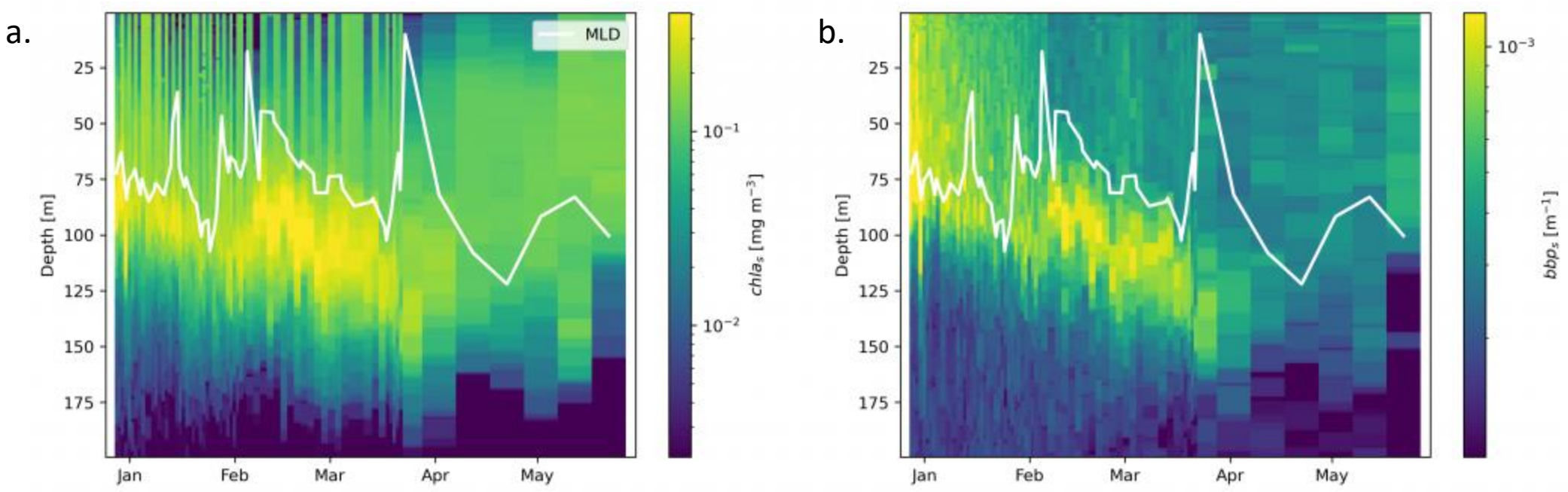
a.
MLD
Depth [m]
25
50
75
100
125
150
175
Jan
Feb
Mar
Apr
May
10^{-1}
10^{-2}
$chla_s$ [mg m^{-3}]
b.
Depth [m]
25
50
75
100
125
150
175
Jan
Feb
Mar
Apr
May
10^{-3}
bbp_s [m^{-1}]

Figure 9 (cont)

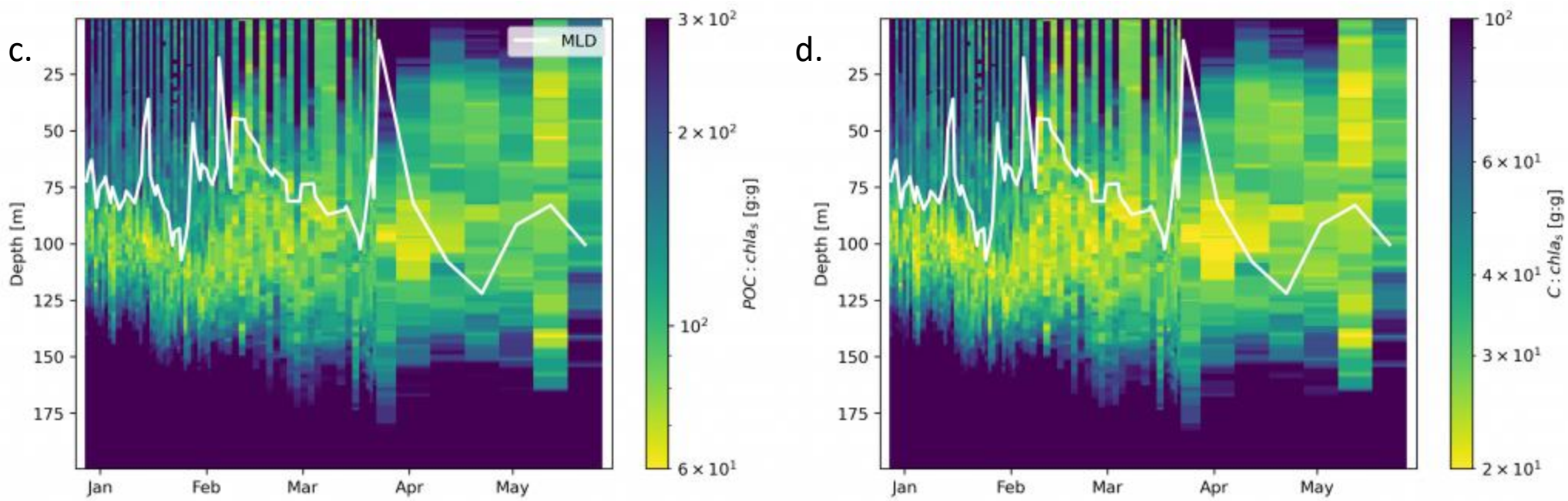

Figure 10

a.

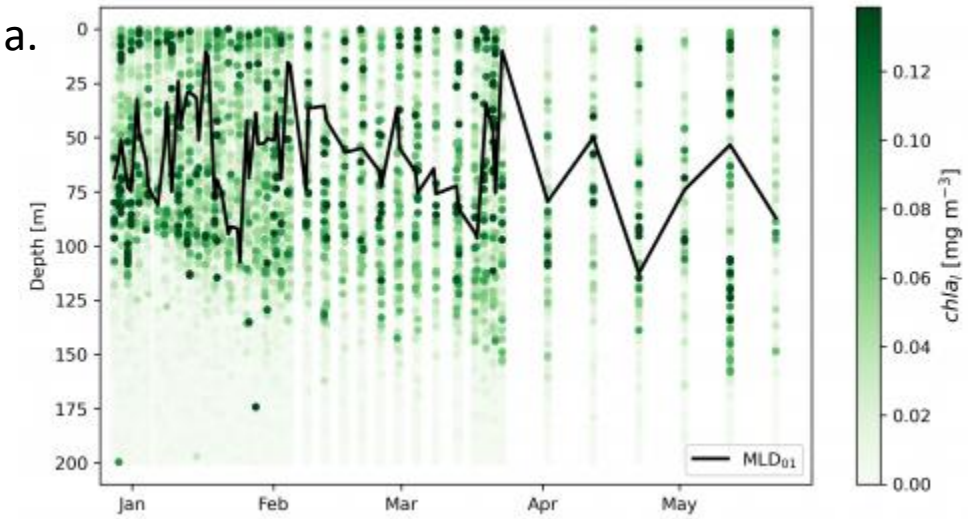
Depth [m]
0
25
50
75
100
125
150
175
200
Jan
Feb
Mar
Apr
May
MLD01
0.12
0.10
0.08
0.06
0.04
0.02
0.00
chla_f [mg m^-3]

b.

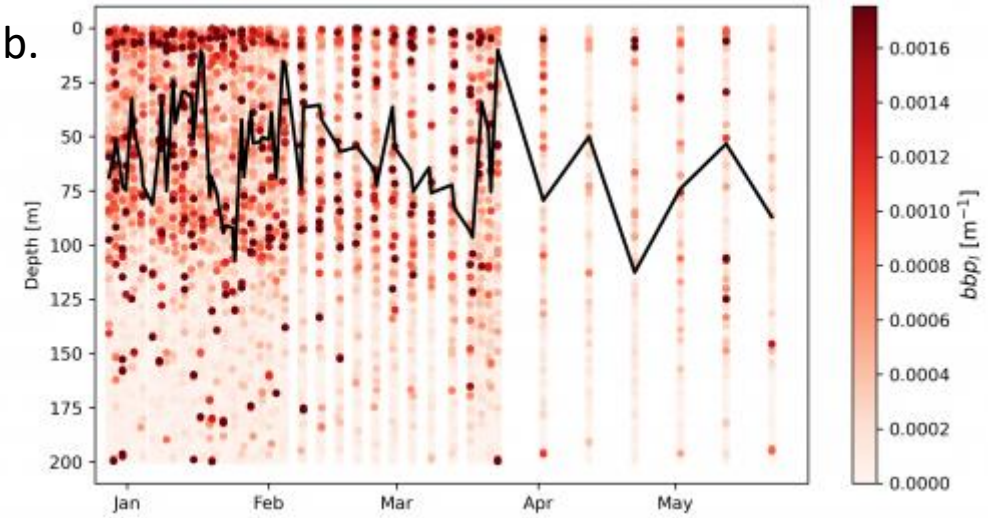
Depth [m]
0
25
50
75
100
125
150
175
200
Jan
Feb
Mar
Apr
May
0.0016
0.0014
0.0012
0.0010
0.0008
0.0006
0.0004
0.0002
0.0000
bbp_f [m^-1]

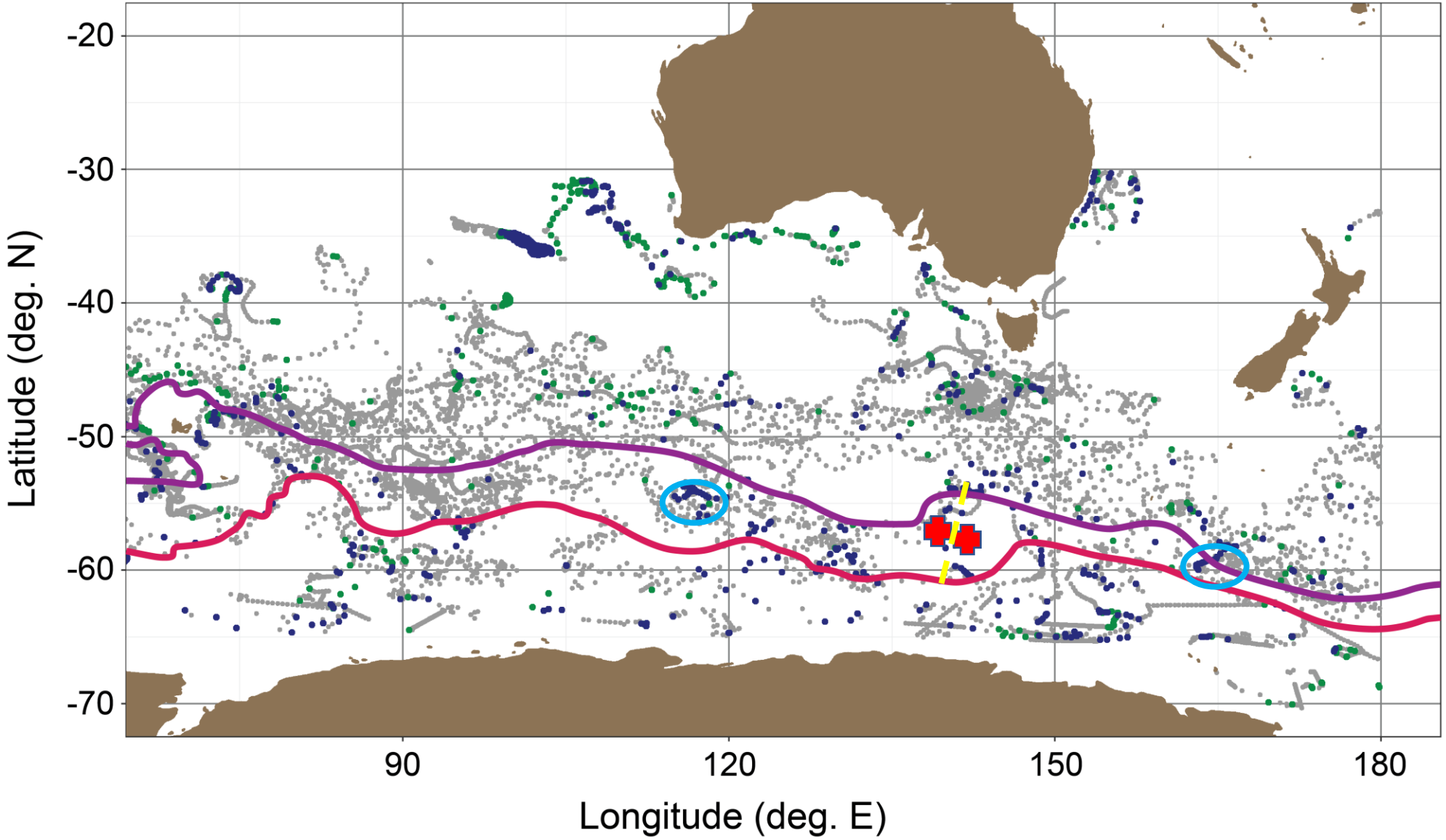

Figure 11

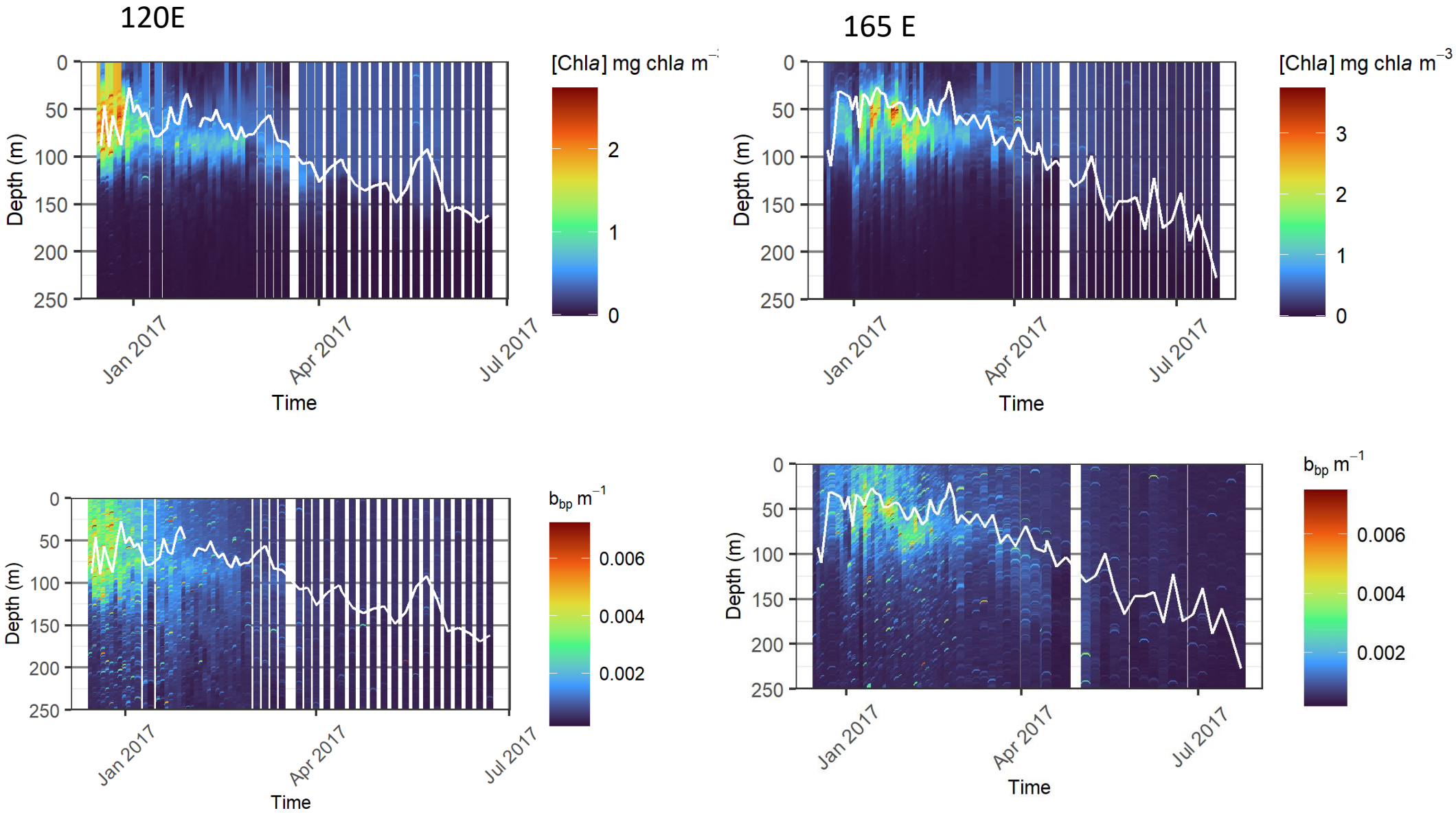
120E
165 E
[Chla] mg chla m^{-3}
Depth (m)
0
50
100
150
200
250
Jan 2017
Apr 2017
Jul 2017
Time
1
2
3
b$_{bp}$ m^{-1}
0.002
0.004
0.006

Figure 12